https://doi.org/10.5194/egusphere-2026-2794
Preprint. Discussion started: 11 June 2026
© Author(s) 2026. CC BY 4.0 License.

# Extracting coherent spatio-temporal modes of simulated multi-centennial AMOC variability under constraints that reflect sparsity of proxy data

Toon Bense[1], Henk A. Dijkstra[2], and Pepijn Bakker[1]

[1]Department of Earth Sciences, Faculty of Science, Vrije Universiteit Amsterdam, Amsterdam, the Netherlands.
[2]Institute for Marine and Atmospheric research Utrecht, Utrecht University, Utrecht, the Netherlands

**Correspondence:** Toon Bense (t.bense@vu.nl)

**Abstract.** A mechanistic understanding of internal variability of the climate is crucial as internal variability has a strong influence on regional to local climate projections throughout the 21st century. The Atlantic Meridional Overturning Circulation (AMOC) strongly impacts regional to local climate and geological evidence suggests (multi-)centennial AMOC variability (mCAV) is a feature of the Mid- to Late Holocene climate. However, our understanding of the spatio-temporal aspects and underlying mechanisms of mCAV is very limited. Understanding the mechanisms behind Holocene mCAV requires a methodology that isolates spatio-temporal patterns of variability and is applicable to both climate model output and the geological archive. Multi-channel singular spectrum analysis (MSSA) has been successfully applied to climate model output to identify and isolate basin-wide spatio-temporal modes of variability. However, it remains unclear if the correct modes can be identified, and if these modes retain their spatio-temporal coherence, when based on input data that is constrained by relatively sparse locations where proxy records are available. Here, we explore this issue in a transient Late Holocene simulation of an earth system model of intermediate complexity that is known to contain mCAV. Our results show that under constrained input data MSSA can be used to identify robust modes of simulated mCAV and that the modes retain their spatio-temporal coherence within at least the northern and eastern North Atlantic. These findings suggest MSSA can be a suitable tool to extract basin-wide modes of variability and associated spatio-temporal patterns from geological reconstructions. This motivates further work that incorporates uncertainties associated with geological reconstructions into the MSSA methodology. Furthermore, our findings motivate the identification and clustering of temperature based phase-relationships in different climate models that contain different mechanisms of mCAV.

https://doi.org/10.5194/egusphere-2026-2794
Preprint. Discussion started: 11 June 2026
© Author(s) 2026. CC BY 4.0 License.

## 1 Introduction

The evolution of the climate system occurs naturally through combinations of changes that are either externally forced or changes that arise through internal variability, or combinations of both. In addition to natural variability, anthropogenic greenhouse gas emissions impose increasingly strong forcings on the climate system. On regional spatial scales, the effects of natural variability can outweigh the effects of anthropogenic climate change in the coming decades (Deser et al., 2012a, b). On local scales, the effects of internal variability remain a significant source of uncertainty in climate projections for 2100 (Lehner and Deser, 2023). As natural variability forms an important source of uncertainty in sub-global scale climate projections that inform policymakers, it is important that it is accurately represented in climate models. However, climate models typically underestimate the natural variability on regional and smaller spatial scales at timescales longer than ∼50 years compared to observational and proxy evidence (Lovejoy et al., 2013; Laepple and Huybers, 2014; Ellerhoff and Rehfeld, 2021; Zhu et al., 2019; Hébert et al., 2022; Laepple et al., 2023). A proposed cause for the model-data mismatch is the absence or underestimation of low-frequency modes of internal variability in climate models (Lovejoy et al., 2013; Ellerhoff and Rehfeld, 2021).

(Multi-)centennial variability of the Atlantic Meridional Overturning Circulation (AMOC) is a potential candidate for such a mode of low-frequency variability. The AMOC is a set of large scale upper ocean currents that transport heat and salt from the Southern Hemisphere to the Northern Hemisphere, and deep ocean currents that return southwards. The AMOC system is known to be strongly variable on timescales ranging from (sub-)seasonal (Kanzow et al., 2010; Marotzke, 2023) to millennial (e.g., Dansgaard et al., 1993) and strongly impacts North Atlantic climate through its northward heat transport. Furthermore, the North Atlantic has been identified as a region of interest regarding (multi-)centennial variability (Taricco et al., 2015; Askjær et al., 2022). It has also been shown that such low-frequency variability likely originates from the oceans and modulates the local terrestrial higher frequency variability (Hébert et al., 2022). (Multi-)centennial AMOC variability (mCAV) related to purely internal dynamics has been shown to be a feature of climate models ranging from the conceptual level (Winton, 1995; Sévellec et al., 2006; Li and Yang, 2022; Yang et al., 2024a) to fully coupled Earth System Models (ESMs) (e.g., Meccia et al., 2023; Jiang et al., 2021; Waldman et al., 2021; Yang et al., 2024b; Mehling et al., 2024). However, other CMIP5 and CMIP6 era ESMs either do not show significant mCAV or lack sufficiently long simulations to identify (multi-)centennial oscillations (Mehling et al., 2024). Analyses of models with mCAV have reported different potential mechanisms, with associated variability originating in different regions, such as the tropical North Atlantic (Vellinga and Wu, 2004), North Atlantic sub-polar region (Yang et al., 2024b), Arctic Ocean (Jiang et al., 2021; Meccia et al., 2023; Mehling et al., 2024), or Southern Ocean (Delworth and Zeng, 2012; Park and Latif, 2008; Latif et al., 2013; Martin et al., 2015). While models can suggest potential mechanisms of mCAV, providing evidence for which of the proposed mechanisms aligns with the real world necessarily relies on the geological record.

There is widespread qualitative evidence of Holocene (multi-)centennial variability in geological proxy records that are associated with the AMOC through archives that reconstruct sea surface temperatures (SSTs) or through archives that represent aspects of the bottom limb of the AMOC (e.g., sortable silt, $\delta^{13}$C) (Moffa-Sánchez et al., 2019). Ayache et al. (2018) applied a principal component analysis (PCA) to Holocene SST records and connected the second empirical orthogonal function

https://doi.org/10.5194/egusphere-2026-2794
Preprint. Discussion started: 11 June 2026
© Author(s) 2026. CC BY 4.0 License.

(EOF) to climate variability on multi-centennial timescales. Taricco et al. (2015) performed univariate and multivariate spectral analyses on extratropical Northern Hemisphere temperature records from the Common Era, identifying significant hemisphere-wide (multi-)centennial modes of variability with particular power around the North Atlantic region. Similarly, in a univariate approach, Askjær et al. (2022) showed Holocene SST records from the Atlantic Ocean contain significant spectral power at (multi-)centennial timescales. While proxy-evidence suggest mCAV exists in the Holocene, thus far it remains unclear how to use the geological record to infer relevant information that could explain the mechanisms behind mCAV.

To address this issue we propose to adopt the framework of Mechanistic Indicators (Te Raa et al., 2004; Dijkstra et al., 2006). The framework is based on the principle that a specific mechanism associated with a mode of variability is characterised by a propagation pattern. Propagation can be described by distinct spatio-temporal relations. For example, Dijkstra et al. (2006) showed phase differences between temperature time-series of different Atlantic Ocean regions can function as mechanistic indicator for a specific mechanism of multi-decadal AMOC variability. In the context of mCAV, models could provide hypotheses based on spatio-temporal relations associated to a mechanism of mCAV. Such hypotheses may then be falsified with data from the geological record. To connect models and the geological archive through spatio-temporal mechanistic indicators requires a shared methodology that can identify coherent spatio-temporal patterns associated with modes of variability in both models and geological data.

Spatio-temporal modes of variability have previously been studied successfully in geo-spatial time series with the multivariate spatio-temporal pattern recognition technique multi-channel singular spectrum analysis (MSSA) (e.g., Plaut and Vautard, 1994; Jiang et al., 1995; Schmeits and Dijkstra, 2000; Groth et al., 2017). However, the application of MSSA to the geological record remains limited to Taricco et al. (2015) and is inherently paired with an orders of magnitude reduction in input data compared to the application of MSSA to model or satellite data. It remains unclear if the correct modes can be identified, and if these modes retain their spatio-temporal coherence, when based on input data that is constrained by relatively sparse locations where proxy records are available.

The primary aim of this study is to explore this issue in the context of (multi-)centennial AMOC variability from the perspective of the perfect modelling world. A secondary aim is to introduce the paleoclimate community to MSSA, show how the method can be applied to study climate variability, and show what steps are necessary to obtain robust results. Here, we simulate the transient climate of the Late Holocene using *i*LOVECLIM and identify modes of (multi-)centennial AMOC variability using conventional spectral methods and MSSA. We extract locations of potentially relevant proxy records from the Common Era and Holocene, and use these locations to subsample the *i*LOVECLIM grid. We explore the effect of sub-sampling the model grid on the ability of MSSA to identify the modes of mCAV that are present in the full model grid. Additionally, we explore if modes of mCAV identified from the sub-sampled grid are coherent in space and time with modes of mCAV extracted from the full model grid. If successful, this motivates future work where MSSA is applied to identify spatio-temporal modes of mCAV in the geological record and to falsify model-based hypotheses.

https://doi.org/10.5194/egusphere-2026-2794
Preprint. Discussion started: 11 June 2026
© Author(s) 2026. CC BY 4.0 License.

## 2 Methods

### 2.1 Data and Model simulations

#### 2.1.1 *i*LOVECLIM

The *i*LOVECLIM (version 1.1.3) is a fully coupled earth system model of intermediate complexity and represents a code branch from the LOVECLIM version 1.2, described by Goosse et al. (2010). The *i*LOVECLIM, and its precursors based on the coupling of ECBILT-CLIO, have previously shown to simulate (multi)-centennial AMOC variability under a variety of conditions (e.g., Schulz et al., 2007; Friedrich et al., 2010; Kessler et al., 2020; Bakker et al., 2022), making it a suitable tool for the purposes of this study.

The activated components in our model simulation include models for the ocean and sea-ice, atmosphere, vegetation, and ocean carbon cycle. The ocean and sea-ice component (CLIO) has a free-surface with horizontal resolution of 3° and 20 vertical layers of increasing thickness downwards (Goosse et al., 2010). Isopycnal mixing and the Gent and McWilliams (1990) eddy parametrisation are used. Open ocean convection is enforced by increasing the vertical diffusivity for water columns that are unstable over at least 100 metres (Goosse et al., 2010). The overflow waters are parametrised such that dense shelf waters flow downslope to depths of equal density (Campin and Goosse, 1999). The ocean carbon cycle model is from Bouttes et al. (2015), and includes the Pa/Th module from Missiaen et al. (2020). The atmospheric component ECBILT is a quasi-geostrophic model with a $\sim$5.6° horizontal resolution resolved at 800, 500, and 200 $\mathrm{hPa}$. The VECODE component models vegetation and terrestrial carbon fluxes (Brovkin et al., 1997).

To more closely capture the dynamics that affected proxy records during the mid-late Holocene, we simulate the transient climate between 6000 to 0 $\mathrm{yr}$ before present (BP). The simulation is a spin-off from a 3000 $\mathrm{yr}$ equilibrium simulation with constant forcings of 6000 $\mathrm{yr\,BP}$. The forcings include greenhouse gas forcings ($CO_2$, $CH_4$, $N_2O$) derived from ice cores (Raynaud et al., 2000; Schilt et al., 2010) and insolation forcings related to the variations in orbital configuration (Berger, 1978). The ice-sheets are kept at their fixed pre-industrial conditions. Similarly, we do not include variable solar and volcanic forcings in the simulation. Even though both forcings have been suggested to influence (multi-)centennial variability (Sarnthein et al., 2003; Salzer et al., 2014; Anchukaitis et al., 2017; Moffa-Sánchez et al., 2014; Slawinska and Robock, 2018; Zhong et al., 2011), we deem our approach an appropriate simplification as a data-model comparison is outside the scope of this study. In this work, we use the final 3000 $\mathrm{yr}$ of the transient simulation. We use decadally averaged temperature and salinity fields to reduce computational costs and limit the analysis to the Atlantic and Arctic basins (Fig. 1). Decadal averages may mask high-frequency variability but we do not expect it to impact the identification of (multi-)centennial oscillatory processes as a decadal sampling rate remains well within the Nyquist frequency.

#### 2.1.2 Proxy location data

To identify the location of potentially relevant proxy-records, we extract the latitude and longitude from marine temperature proxy reconstructions included in the PAGES 2k temperature database (PAGES2k Consortium et al., 2017) (version 2.2.0)

https://doi.org/10.5194/egusphere-2026-2794
Preprint. Discussion started: 11 June 2026
© Author(s) 2026. CC BY 4.0 License.

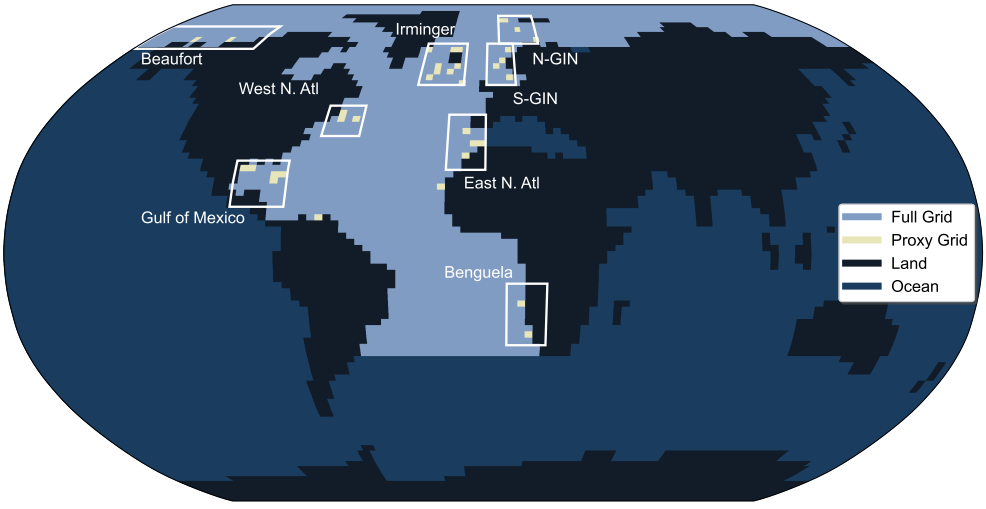


**Figure 1.** *i*LOVECLIM grid. The Full Grid area reflects the MSSA input data and is limited to the Atlantic Ocean (north of 34.5 °S) and Arctic Ocean. The land and remaining ocean cells are not used in the MSSA analysis. The Proxy Grid reflects the 35 ocean grid cells where geological data is available that satisfies the criteria described in Sect. 2.1.2. The white boxes and annotations outline the boundaries of the sectors that are used to compute time-series (see Sect. 3.5).

and the temperature 12k database (Kaufman et al., 2020) (version 1.0.0). We only use the locations of temperature records from marine sediments located within the Arctic Ocean or Atlantic Ocean north of 30°S. We add an additional constraint of a maximum average sampling interval of 100 yr as a first order criteria to select records that could potentially contribute to detection of (multi-)centennial variability. After removal of duplicates, 61 locations remain (Tables. A1,A2,A3), which fall within 35 ocean grid cells of the *i*LOVECLIM grid (Fig. 1). These grid cells are used in further analysis and are referred to as the Proxy Grid.

## 2.2 Analysis methods

### 2.2.1 MSSA: conceptual explanation

Multi-channel singular spectrum analysis is a relatively unknown methodology within paleoclimate research. It can be useful to think of MSSA as a combination of the more known singular spectrum analysis (SSA) and principal component analysis (PCA). In this section we qualitatively cover the different use cases and advantages of the three methods in the context of climate variability. In the next section (Sect. 2.2.2), we provide a more detailed mathematical introduction to MSSA to those

https://doi.org/10.5194/egusphere-2026-2794
Preprint. Discussion started: 11 June 2026
© Author(s) 2026. CC BY 4.0 License.

who are interested. To provide an explanation of the similarities and differences between SSA, PCA and MSSA the methods are applied within the context of the El Niño Southern Oscillation (ENSO) (Fig. 2). All three methods have previously been applied to ENSO, e.g., SSA Rasmusson et al. (1990); Keppenne and Ghil (1992), PCA Ashok et al. (2007), and MSSA Jiang et al. (1995). We use monthly SSTs from HadISST (1.1) from 1951-1994 over the tropical Pacific Ocean (20°N - 20°S, 150°E - 80°W) (Rayner et al., 2003). Prior to application, we detrend the data with a second order polynomial followed by standardisation to z-scores.

SSA is a method that is applied to single time-series to identify and filter the temporal patterns (Broomhead and King, 1986a, b; Vautard and Ghil, 1989). These patterns are associated with specific frequencies, making SSA function as a spectral analysis method. If multiple oscillations at different frequencies are identified, these can be considered distinct modes of variability. E.g., when applied to the Niño3 index (Fig. 2a), there are pairs of eigenvalues (blue markers) around the frequencies $\sim$0.02 and 0.04 $\mathrm{months}^{-1}$ (Fig. 2b), which are indicative of oscillations (Allen and Smith, 1996). Section 2.2.2 contains a more detailed description on identification of oscillations in (M)SSA spectra. The $\sim$0.02 and 0.04 $\mathrm{months}^{-1}$ modes correspond to periods of $\sim$46 and 26 $\mathrm{months}$ and are linked to the quasi-quadrennial and quasi-biennial modes of ENSO (Keppenne and Ghil, 1992; Rasmusson et al., 1990). Aside from identifying modes, SSA can be used to reconstruct filtered versions of the time-series that correspond to the identified oscillation. E.g., the blue line in Figure 2a is the filtered Niño3 time-series associated with the quasi-quadrennial mode. An inherent limitation of SSA is that it is univariate and can therefore not be used to infer spatial or spatio-temporal information.

Within the context of climate variability, PCA is applied to a set of geospatial time-series to identify the spatial patterns that explain most of the variance (Preisendorfer and Mobley, 1988). Additionally, PCA is used to determine the temporal evolution of the amplitude of the spatial patterns. E.g., when applied to equatorial Pacific SST anomalies (Fig. 2c), PCA identifies the spatial pattern shown in Fig. 2f, which represents the classical ENSO mode (e.g., Ashok et al., 2007; Rasmusson and Carpenter, 1982). Figure 2g shows the temporal evolution associated with the amplitude of the spatial pattern. In theory, combining the spatial pattern and its temporal evolution gives a set of geospatial time-series that reflect how the spatial pattern changes in amplitude over time. However, as the spatial-pattern is fixed this approach only provides limited information about the underlying mechanisms of the variability. Another limitation of PCA is that different modes of variability cannot be separated if the modes have spatial features in common.

MSSA overcomes the limitations of SSA and PCA when used to study modes of climate variability. MSSA is applied to a set of geospatial time-series to identify patterns in space and time (Broomhead and King, 1986a, b; Vautard and Ghil, 1989; Plaut and Vautard, 1994). Like in SSA, the patterns are associated with specific frequencies which can lead to identification of distinct modes of variability. E.g., when applied to equatorial Pacific SST anomalies (Fig. 2c), there are significant pairs of eigenvalues around the frequencies 0.02 and 0.04 (Fig. 2d), which are linked to the quasi-quadrennial and quasi-biennial modes of ENSO (Jiang et al., 1995). Aside from identifying modes in multivariate datasets, MSSA can be used to reconstruct filtered versions of the set of geospatial time-series that correspond to the identified patterns. E.g., Fig. 2e shows the evolution in space and time of the filtered signal associated with the quasi-quadrennial mode. Critically, the filtered spatio-temporal

https://doi.org/10.5194/egusphere-2026-2794
Preprint. Discussion started: 11 June 2026
© Author(s) 2026. CC BY 4.0 License.

patterns evolve in both amplitude and structure over time and are therefore suitable to study the mechanisms of the mode of variability.

### 2.2.2 MSSA: mathematical explanation

Here, we introduce the mathematical foundation behind SSA, PCA and MSSA, and show how MSSA combines the advantages of both SSA and PCA. The three methods are based on the same mathematical principle. The methods solve an eigenvalue problem, where a covariance matrix C is diagonalised to obtain eigenvectors $E$ and eigenvalues $\Lambda$ (Preisendorfer and Mobley, 1988; Broomhead and King, 1986a, b; Allen and Robertson, 1996), i.e.,

$$\Lambda = E^T C E \tag{1}$$

where $E^T$ indicates the transpose of matrix $E$. The structure of the covariance matrix differs between the methods, resulting in eigenvectors that contain different statistical information while the eigenvalues are always a measure of the amount of variance that is explained by their associated eigenvectors. We first introduce how the covariance matrices for SSA and PCA are built, and then show how the MSSA covariance matrix is based on aspects of SSA and PCA. Additionally, we show how the information contained in the eigenvectors of the three methods differs and how they are typically used in the context of climate variability.

SSA is typically used to identify and filter the leading temporal patterns of a time-series, such as trends or oscillations. SSA is applied to a single time-series $x$ of length N ($x_{n:1,N}$), e.g., Niño3 (Fig. 2a). SSA is based on a sliding window approach to build a trajectory matrix $X_{SSA}$ of size ($N' \times M$) built with $N' = N - M + 1$ lagged copies of time-series $x$, where each copy is of a window size $M$ (Broomhead and King, 1986a, b; Allen and Robertson, 1996), giving

$$X_{SSA} = \begin{bmatrix} x_{n=1} & x_{n+1} & x_{n+2} & \dots & x_M \\ x_{n+1} & x_{n+2} & x_{n+3} & \dots & x_{M+1} \\ \vdots & \vdots & \vdots & \ddots & \vdots \\ x_{N'=N-M+1} & x_{N'+1} & x_{N'+2} & \dots & x_N \end{bmatrix} \tag{2}$$

The M x M lag-covariance matrix $C_{SSA} = \frac{X^T X}{N'}$ is determined and diagonalised according to Eq. (1). The eigenvectors are known as time empirical orthogonal functions (T-EOFs) and represent temporal patterns captured within the window $M$. Projecting the time-series $x$ onto the T-EOFs yields time-principal components (T-PCs), which indicate the amplitude of the temporal pattern within the sliding window $N'$ (Ghil et al., 2002). A Fourier analysis can be used to estimate the dominant frequency of each T-EOF. The eigenvalue of each T-EOF is combined with its associated frequency to construct the SSA spectrum. E.g., the SSA spectrum for the Niño3 time-series (Fig. 2b) shows eigenvalues of the T-EOFs plotted against their associated frequency.

There are three criteria to identify potential oscillations in a SSA spectrum (Plaut and Vautard, 1994; Allen and Smith, 1996) and these criteria also apply to MSSA spectra (Allen and Robertson, 1996). First, oscillations are characterised by a pair of

https://doi.org/10.5194/egusphere-2026-2794
Preprint. Discussion started: 11 June 2026
© Author(s) 2026. CC BY 4.0 License.

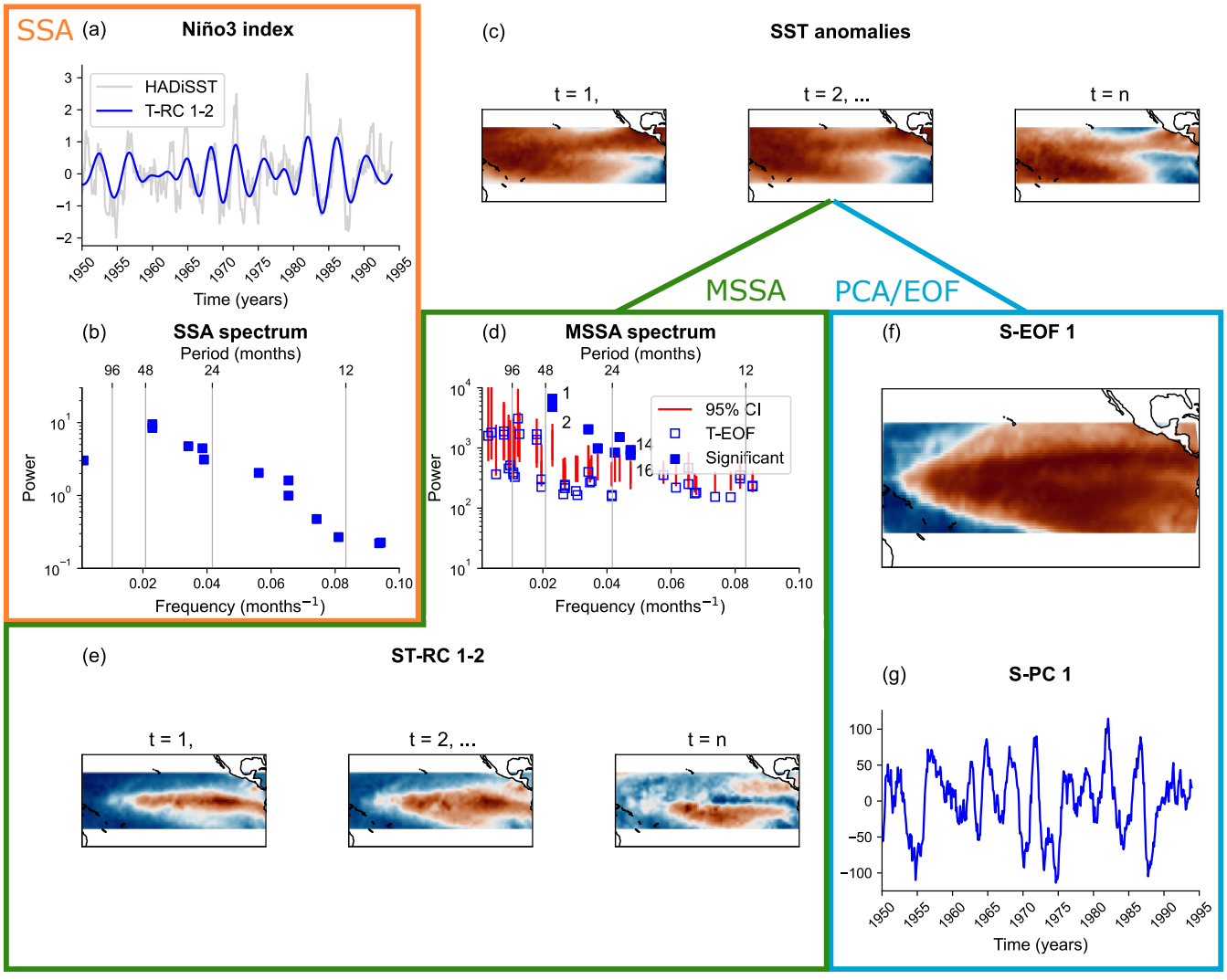


**Figure 2.** Example of the methods SSA, PCA, and MSSA applied within the context of ENSO. a) Raw Niño3 time-series in grey (SSA input data) and SSA filtered quasi-quadrennial time-series (T-RC 1-2, blue) associated with the T-EOF pair at 48 months in panel b. b) SSA spectrum, where the eigenvalues are plotted against the dominant frequency of the associated eigenvector. Oscillations are indicated by pairs of T-EOFs that meet the frequency, quadrature, and power criteria (section 2.2.2), such as the T-EOF pair at a period of 48 months. c) Pacific SST anomalies that represent an example of PCA and MSSA input data at different timesteps. Each grid cell represents a channel d in matrix $P$ (Eq. (3)). d) MSSA spectrum, where the eigenvalues are plotted against the dominant frequency of the associated eigenvector. Red bars indicate the 95% confidence intervals from the red noise based significance test. Oscillations are indicated by pairs of significant T-EOFs that meet the frequency, quadrature, and power criteria (Sect. 2.2.2). e) Filtered quasi-quadrennial signal (ST-RC 1-2) associated with T-EOF pair 1-2 at 48 months in panel d. f) pattern from the PCA analysis (S-EOF 1), representing the spatial features of ENSO that explain most variance. g) Temporal evolution that reflects how the amplitude of the associated spatial pattern in panel f changes over time.

https://doi.org/10.5194/egusphere-2026-2794
Preprint. Discussion started: 11 June 2026
© Author(s) 2026. CC BY 4.0 License.

T-EOFs that share the same dominant frequency. Second, there is a phase shift between the two T-EOFs that equals a quarter of the period, known as being in quadrature. Third, the two T-EOFs have similar power, meaning a similar eigenvalue. These criteria can most easily be understood when a T-EOF pair is though of as a sine-cosine pair. By definition, such a pair shares the same frequency and is in quadrature. If the amplitudes of the pair remain constant over time, both will have the same amplitude, explain the same variance, and hence have the same power. However, differences in power between members of a T-EOF pair may form due to e.g., amplitude modulation or intermittency. Note that T-EOFs are not constrained by specific wave shapes and can therefore capture non-linear behaviour (Vautard and Ghil, 1989; Ghil et al., 2002). Additionally, T-EOFs are not constrained by predetermined frequencies and (M)SSA will only find T-EOFs at frequencies where variance exists in the data.

As an example, we apply the oscillatory criteria to the SSA spectrum for the Niño3 index (Fig. 2b), where we find T-EOF pairs of equal frequency at frequencies of e.g., $\sim$0.02, 0.04 $\mathrm{months}^{-}1$. The two pairs are associated with periods of $\sim$46 and 26 $\mathrm{months}$, and are both in quadrature (not shown). The 26 month pair is not of the exact same power, though the difference is relatively small. These T-EOF pairs have previously been linked to the quasi-quadrennial and quasi-biennial modes of ENSO (e.g., Rasmusson et al., 1990; Keppenne and Ghil, 1992). Once a T-EOF pair has been identified as a mode of variability, it can be used to compute the time reconstructed component (T-RC), which is a filtered version of the original time-series. E.g., we select T-EOF 1-2 associated with the 46 month period and compute T-RC 1-2, which represents the filtered time-series associated with the quasi-quadrennial ENSO mode (Fig. 2a).

In the context of climate variability, principal component analysis is often used to identify the leading spatial patterns within a set of geo-spatial time-series. The set of geo-spatial time-series can be represented by a matrix $P$ of size $N \times D$, where $D$ represents the amount of time-series (or locations) and $N$ the length of the time-series (e.g., the Pacific SST anomalies in Fig. 2c) (Preisendorfer and Mobley, 1988). In the context of general PCA use, the locations of the time-series ($D$) are the "variables" and the timesteps (N) are the "samples". The matrix $P$ given by

$$P = \begin{bmatrix} x_{n=1,d=1} & x_{n=1,d=2} & x_{n=1,d=3} & \cdots & x_{n=1,d=D} \\ x_{n=2,d=1} & x_{n=2,d=2} & x_{n=2,d=3} & \cdots & x_{n=2,d=D} \\ x_{n=3,d=1} & x_{n=3,d=2} & x_{n=3,d=3} & \cdots & x_{n=3,d=D} \\ \vdots & \vdots & \vdots & \ddots & \vdots \\ x_{n=N,d=1} & x_{n=N,d=2} & x_{n=N,d=3} & \cdots & x_{n=N,d=D} \end{bmatrix} \tag{3}$$

is used to compute the covariance matrix $C_{PCA} = \frac{P^T P}{N-1}$. The diagonalization of $C_{PCA}$ (Eq. ( 1)) yields eigenvectors referred to as space empirical orthogonal functions (S-EOFs). In terms of a general PCA, the S-EOFs are the "loadings" that explain how the locations (variables) co-vary. S-EOFs thus represent spatial patterns that explain most variance in the dataset. E.g., PCA applied to equatorial Pacific SST anomalies results in the spatial pattern S-EOF-1 (Fig. 2f) associated with the classical ENSO mode (e.g., Ashok et al., 2007; Rasmusson and Carpenter, 1982). Projection of $P$ onto the S-EOFs yields the associated space principal components (S-PCs). In terms of a general PCA, the S-PCs are the "scores" that explain how strong a spatial

https://doi.org/10.5194/egusphere-2026-2794
Preprint. Discussion started: 11 June 2026
© Author(s) 2026. CC BY 4.0 License.

pattern is at each timestep (sample) (Fig. 2g). S-PCs thus describe the temporal evolution associated with the amplitude of the S-EOFs. While the S-PC captures the temporal evolution of the S-EOF, the spatial pattern of a S-EOF always remains fixed. Consequently, PCA provides limited information about the underlying mechanisms of variability. Additionally, PCA does not identify distinct modes in frequency-space as no lags are considered in the construction of the covariance matrix. Consequently, if multiple modes exist that share similar spatial features they cannot be separated with PCA.

MSSA combines the ability of SSA to identify specific modes of variability in frequency space with the ability of PCA to analyse a full set of geo-spatial time-series, and hence include spatial information. Additionally, once a mode has been identified, MSSA can be used to reconstruct the filtered set of geospatial time-series related to the identified mode. MSSA uses a set of geo-spatial time-series as input data (e.g., matrix $P$ (Eq. ( 3)), similar to PCA. MSSA is the multi-variate extension of SSA which is reflected in the application of a sliding window in the construction of the trajectory matrix. In MSSA, this matrix is built by creating $D$ trajectory matrices $\tilde{X}_{SSA(d)}$ (Eq. 2) for each time-series $1 \leq d \leq D$ (Broomhead and King, 1986a, b; Allen and Robertson, 1996). The individual matrices $\tilde{X}_{SSA(d)}$ are stacked horizontally resulting in a matrix

$$X_{MSSA} = \left[ \begin{array}{cccc} \tilde{X}_{SSA(d=1)} & \tilde{X}_{SSA(d=2)} & \cdots & \tilde{X}_{SSA(d=D)} \end{array} \right]$$

of size $(N', M \times D)$. The computation of the spatio-temporal covariance matrix $C_{MSSA}$ depends on the rank of the trajectory matrix $X_{MSSA}$ (Allen and Robertson, 1996), according to

$$\text{Full rank} : N' > M \times D : C_{MSSA} = \frac{X^T X}{N'}$$

$$\text{Rank-deficient} : N' < M \times D : C_{MSSA} = \frac{X X^T}{MD}$$

Aside from eigenvalues, the diagonalisation of $C_{MSSA}$ (Eq. (1)) yields eigenvectors known as space-time EOFs (ST-EOFs) in the full rank case, and T-EOFs in the rank-deficient case. The other EOFs can always be obtained through projection of $X_{MSSA}$ onto the already obtained eigenvectors (Allen and Robertson, 1996). Alternatively, a singular value decomposition of $X_{MSSA}$ can yield the T-EOFs, ST-EOFs, and singular values ($\Lambda^{1/2}$) directly.

The T-EOFs and eigenvalues can be used to make the MSSA spectrum, where the signal is split in frequency-space and potential modes of variability can be identified. Like in SSA, potential oscillations are characterised by T-EOF pairs that meet the frequency, quadrature, and power criteria (Allen and Smith, 1996; Allen and Robertson, 1996). E.g., the MSSA spectrum for the equatorial Pacific SST anomalies (Fig. 2d) shows several T-EOF pairs of the same frequency and of roughly similar power at periods of ∼11, 13, 22, 48, 56 $\mathrm{months}$ and more. Three out of the five pairs are in quadrature (not shown) but these criteria are not yet sufficient to identify the three modes as oscillatory signal, as similar structures can result from noise (Allen and Smith, 1996). To reduce the chance of identifying false positives, Allen and Smith (1996) and Allen and Robertson (1996) developed a Monte Carlo (MC) significance test for (M)SSA, which was later improved by Groth and Ghil (2015).

The MC-significance test is based on a null-hypothesis that states that each of the D input channels is generated through a first order autoregressive model (AR1), commonly known as a red noise process (Allen and Smith, 1996). In a red noise process, the next value of a time-series is based on a combination of the previous value and of a purely stochastic value. A red

https://doi.org/10.5194/egusphere-2026-2794
Preprint. Discussion started: 11 June 2026
© Author(s) 2026. CC BY 4.0 License.

noise time-series is characterised by increasing spectral power at lower frequencies, and is a good fit for mid-latitude SST fields (Hasselmann, 1976; Frankignoul and Hasselmann, 1977). In the MC-significance test, red noise parameters are estimated for each eigenvector and used to create ensembles of surrogate data. The ensemble of surrogate data is used to construct confidence intervals for each eigenvector, which can be compared to the data eigenvalue (Allen and Robertson, 1996; Allen and Smith, 1996; Groth and Ghil, 2015). When the MC significance test is applied to the MSSA spectrum, only the T-EOF pairs 1-2 and 14-16 associated with periods of 48 and 22 $\mathrm{months}$ remain significant (Fig. 2d). These eigenvector pairs match the additional criteria of frequency, quadrature (not shown), and power and can therefore be considered modes of variability. The 48 and 22 month modes are associated with the quasi-quadrennial and quasi-biennial modes of ENSO (Jiang et al., 1995).

Upon a selection of an eigenvalue pair, the associated ST-EOFs are used to compute the space-time principal components (ST-PCs) and reconstructed components (ST-RCs) (see Ghil et al. (2002) for details). The ST-RCs represent the filtered mode of variability in the dimensions of the original dataset $P$. E.g., the ST-RC pair 1-2 shown in Fig. 2e are filtered geospatial time-series from the original SST-anomalies shown in Fig. 2c related to the quasi-quadrennial T-EOF pair 1-2 from the MSSA spectrum in Fig. 2d. The ST-RCs vary in amplitude and structure over time and can therefore be a powerful method to study the mechanism of the spatio-temporal behaviour of a mode.

#### 2.2.3 MSSA: pre-processing and analysis choices

Here, we describe the specific pre-processing and analysis choices that we apply to the *i*LOVECLIM data to study mCAV using MSSA. Prior to analysis, we detrend each time-series with a second order polynomial as the forcings in the transient simulation change over time. However, note that detrending is not strictly required prior to MSSA as trends can be identified by eigenvectors within the analysis (e.g., Groth et al., 2017). It is standard practice to standardise the time-series to z-scores and to perform an initial PCA analysis in which a number of leading S-PCs are retained to reduce dimensionality and impose orthogonality (Allen and Robertson, 1996; Groth and Ghil, 2015). However, selecting too few S-PCs can lead to failed identification of signals within the significance testing procedure (Groth and Ghil, 2015). To prevent unnecessary false negatives, we follow the recommendation by Groth et al. (2017) and use the maximum number of available S-PCs. Together, the S-PCs form the input matrix $P$. MSSA can be applied to several variables at the same time to explore how the variables covary together in space and time. In such a joint MSSA, we perform the initial PCA analysis separately for both variables and then stack the S-PCs from both variables together into a single input matrix $P$.

An important consideration in any application of MSSA is the choice of window size $M$. With a larger window, MSSA can better resolve separate peaks that are close together in the spectrum (Plaut and Vautard, 1994). However, increased spectral resolution comes at the cost of temporal resolution resulting in spatio-temporal patterns that are temporally less precise (Plaut and Vautard, 1994). Additionally, with a larger window size the confidence in the statistical test decreases as there are less repetitions of the patterns captured in $M$ throughout the time-series $N$, reflected by the ratio $N/M$ (Ghil et al., 2002). Recent studies have used minimum $N/M$ ratios of $\sim$3.5 and 4 (Groth et al., 2017; Manta et al., 2024), hence we adopt a similar minimum ratio of 3.5. A final consideration in choosing $M$ is the period of interest, as MSSA cannot robustly detect oscillations longer than the window size $M$(Plaut and Vautard, 1994). Here, we choose the initial window size based on a standard spectral

https://doi.org/10.5194/egusphere-2026-2794
Preprint. Discussion started: 11 June 2026
© Author(s) 2026. CC BY 4.0 License.

analysis of the AMOC time-series and follow the suggestion from Plaut and Vautard (1994) to choose $M$ such that the period of interest lies in the interval covered by $[M/5, M]$. It is important to consider that MSSA results can be sensitive to the chosen window size. Of particular importance are eigenvector pairs that are separated in the MSSA spectrum by a frequency distance of $1/M$, which cannot directly be considered separate modes (Allen and Robertson, 1996; Ghil et al., 2002). Therefore, it is important to determine the sensitivity of the MSSA based identification of potential eigenvalue pairs to the chosen window size by repeating the analysis with different values for $M$ (e.g., Allen and Robertson, 1996; Allen and Smith, 1996; Ghil et al., 2002; Schmeits and Dijkstra, 2000; Manta et al., 2024).

Generally, the criteria of frequency, quadrature, and power are interpreted from plots such as the MSSA spectrum. To retain consistency across analysing a large amount of MSSA spectra, we automate the process in a heuristic way. First, we identify pairs of equal frequency that consist of two significant T-EOFs. For each significant T-EOF, we consider combinations with the next 5 significant T-EOFs. To meet the criterium, both T-EOFs must fall within the frequency interval $[1/(T_{av} \pm 0.025 \times T_{av})]$, where $T_{av}$ is the average period of the two considered T-EOFs. To meet the power criterium, both members of the T-EOF pair must fall within the interval $[\lambda_{av} \pm 0.025\lambda_{av}]$, where $\lambda_{av}$ is the average eigenvalue of the two T-EOFs. To meet the quadrature criterium, the phase shift $\Phi$ between the two T-EOFs must fall within the interval $[\Phi_{lower}, \Phi_{upper}]$ indicated by $[0.25 \pm 0.025 \times T_{av}]$. However, the $[\Phi_{lower}, \Phi_{upper}]$ requires an additional constraint to ensure there is at least a 1-index range considered as quadrature in the decadally averaged data, which is achieved through a floor and ceiling function.

$$\Phi_{lower} = min \begin{cases} 0.25 - 0.025 \times T_{av} \\ floor(\frac{0.25 \times T_{av}}{10}) \times 10 \end{cases}$$

$$\Phi_{upper} = max \begin{cases} 0.25 + 0.025 \times T_{av} \\ ceiling(\frac{0.25 \times T_{av}}{10}) \times 10 \end{cases}$$

In addition, the standard MSSA algorithm is complemented with the varimax rotation from Groth and Ghil (2011) to increase the separability of modes. The varimax rotation is applied to all ST-EOFs that explain more than 1% of the variance. Also, the Groth and Ghil (2015) significance test is applied, which includes a scaled Procrustes target rotation to the T-EOFs, a modification of the original significance test (Allen and Robertson, 1996; Allen and Smith, 1996). Unless mentioned otherwise, the significance test is based on 1000 Monte Carlo realisations and T-EOFs are considered significant if they exceed the $99^{th}$ percentile of the surrogate data.

#### 2.2.4 Standard spectral analysis

Here, spectral analyses of the annual AMOC time-series are based on the multi-taper method (MTM) (Percival and Walden, 2020; Thomson, 1982) and wavelet analysis (Torrence and Compo, 1998). The MTM contains a significance test based on a null hypothesis of a red noise spectrum, which is fit to the median-smoothed data power spectrum ($\Delta f_{smooth}$ = 0.05 year$^{-1}$ (Mann and Lees, 1996). The wavelet analysis uses a Morlet wavelet ($\omega$ =6) and the Liu et al. (2007) bias correction for oceanic data is applied to the power spectrum. The wavelet analysis also contains a significance test based on a red noise power spectrum,

https://doi.org/10.5194/egusphere-2026-2794
Preprint. Discussion started: 11 June 2026
© Author(s) 2026. CC BY 4.0 License.

which is fit on the lag-1 autocorrelation coefficient of the time-series. In the wavelet analysis, significance is determined based on a $\chi^2$ distribution with 2 degrees of freedom (Torrence and Compo, 1998). For both spectral analyses, we first detrend the data with a second order polynomial, and then standardise the data to z-scores.

https://doi.org/10.5194/egusphere-2026-2794
Preprint. Discussion started: 11 June 2026
© Author(s) 2026. CC BY 4.0 License.

## 3 Results

### 3.1 (Multi-)centennial AMOC variability

We determine the presence and periodicities of the AMOC variability in the late Holocene simulations by applying spectral analyses directly to the AMOC time-series. The spectral analyses inform the choice of the MSSA window size $M$ and act as a baseline to compare the MSSA results to.

The AMOC strength (Fig. 3a), defined as the maximum meridional overturning in the North Atlantic between 45 °N - 65 °N and below 500 m, in the late Holocene simulation has a mean strength of 15.9 Sv ($10^6 \mathrm{m}^3/\mathrm{s}$), which is slightly lower than the initial PI spin-up simulation (17 Sv, not shown). The 50-yr low-pass filtered time-series shows pronounced variability on (multi)-centennial timescales, with an 1.6 Sv standard deviation and peak-to-peak excursions in the range of 1-7 Sv. The multi-taper spectrum of the raw annual AMOC time-series shows that periods longer than 105 yr contain significant power at the 99% confidence level (Fig. 3b). The broad (multi-)centennial band is characterised by local peaks at periods in the ranges of 130-170 and 200-270 yr, while the highest power is located between periods of 350-600 yr. Additionally, the multi-taper spectrum shows evidence of significant higher-frequency variability at multi-decadal (∼70-80 yr) and decadal (∼15 yr) timescales. The broad (multi)-centennial variability is also reflected in the wavelet power spectrum (Fig. 3c), where at times the full range between 140-600 yr is significant at the 95% confidence level. The lower-frequency (∼500 yr) variability appears as a significant signal throughout the simulation, while the 140-250 yr variability is significant between 2000-1500 yr BP and from 900 yr BP onwards. The wavelet spectrum also shows evidence of increased, but not significant, variability in the multi-decadal to bi-centennial ranges. Sporadically, the wavelet spectrum shows significant power at decadal timescales.

### 3.2 Modes of AMOC variability: zonally averaged perspective

We first apply joint MSSA to the zonally averaged temperature and salinity fields as we expect the signal-to-noise ratio of the mCAV to be highest in the latitude - depth domain (Te Raa and Dijkstra, 2003). We consider joint temperature and salinity fields as buoyancy anomalies are a combination of thermal and haline anomalies. We choose an initial window size $M$ = 500 yr to cover a large range of periodicities (100-500 yr, see Sect. 2.2.3) of the identified (multi-)centennial AMOC variability (Fig. 3).

Figure 4a shows the the MSSA spectrum of the joint zonally averaged salinity and temperature analysis. Five pairs of T-EOFs with the same frequency are significant above the 99% percentile with associated periodicities of ∼440, 280, 200, 140, and 105 yr. The ST-PC pair 5-7 associated with the 200-yr mode is shown in Fig. 4b. ST-PC 5 leads ST-PC 7 by a quarter phase throughout most of the model years, indicating the pair is in quadrature. The other T-EOF pairs are also in quadrature (not shown) and all the pairs are of similar power except for T-EOF 3-6 associated with the 280-yr mode. Notably, the T-EOF pairs associated with the 200 and 140-yr modes are separated by a distance of $1/M$ as indicated by the black horizontal line (Fig. 4a). Consequently, these T-EOF pairs cannot be considered as distinct modes, unless they are robust for different window sizes (e.g., Allen and Robertson, 1996).

https://doi.org/10.5194/egusphere-2026-2794
Preprint. Discussion started: 11 June 2026
© Author(s) 2026. CC BY 4.0 License.

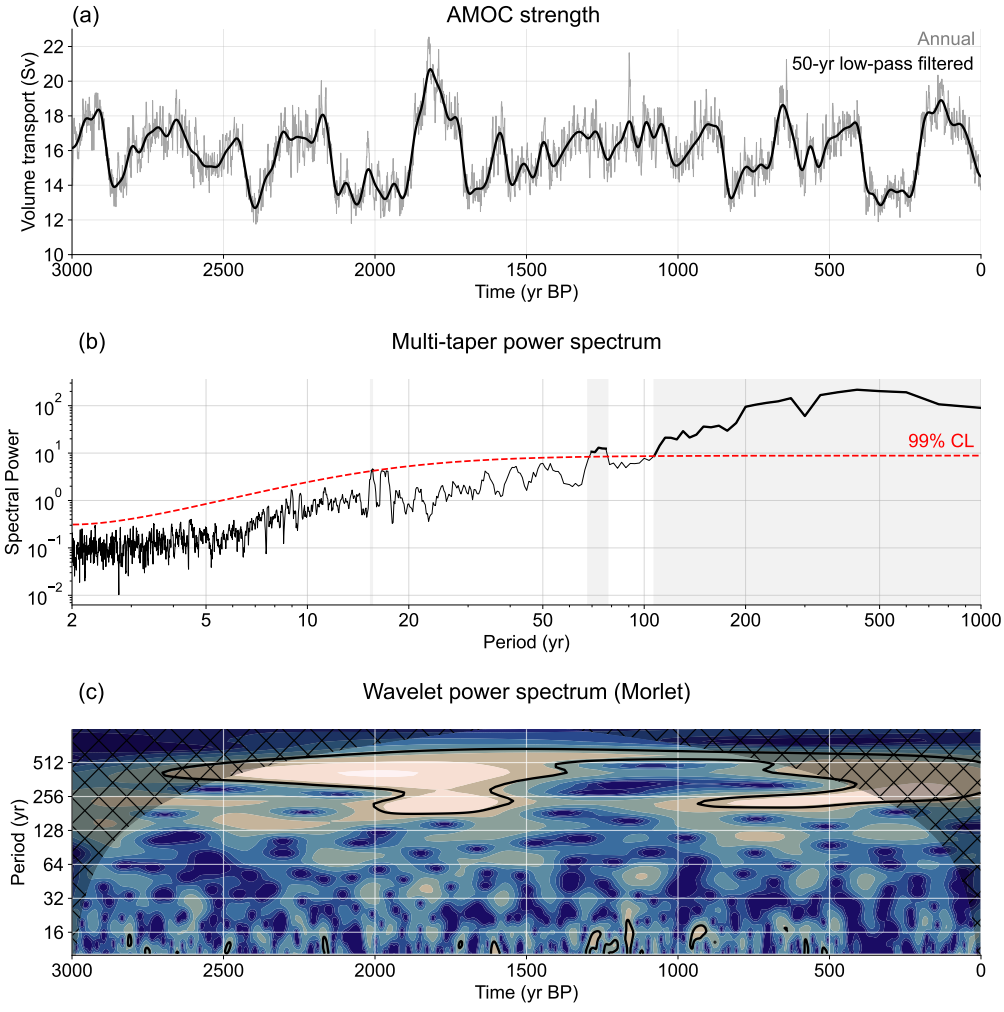


**Figure 3.** AMOC behaviour during the transient Late Holocene simulation. a) Annually averaged AMOC time-series (grey) and 50-yr low-pass filtered time-series (black). b) Multi-taper power spectrum associated with the AMOC time-series. 99% confidence level indicated by red-dashed line. Shaded areas indicate ranges of significant power. c) Wavelet power spectrum associated with the AMOC time-series. Regions that exceed the 95% confidence level are outlined by black contours. Regions that are affected by edge effects are indicated by the hatched areas (Torrence and Compo, 1998). The AMOC strength shows clear (multi-)centennial variability as indicated by the significant spectral power at (multi-)centennial timescales in panels b) and c).

https://doi.org/10.5194/egusphere-2026-2794
Preprint. Discussion started: 11 June 2026
© Author(s) 2026. CC BY 4.0 License.

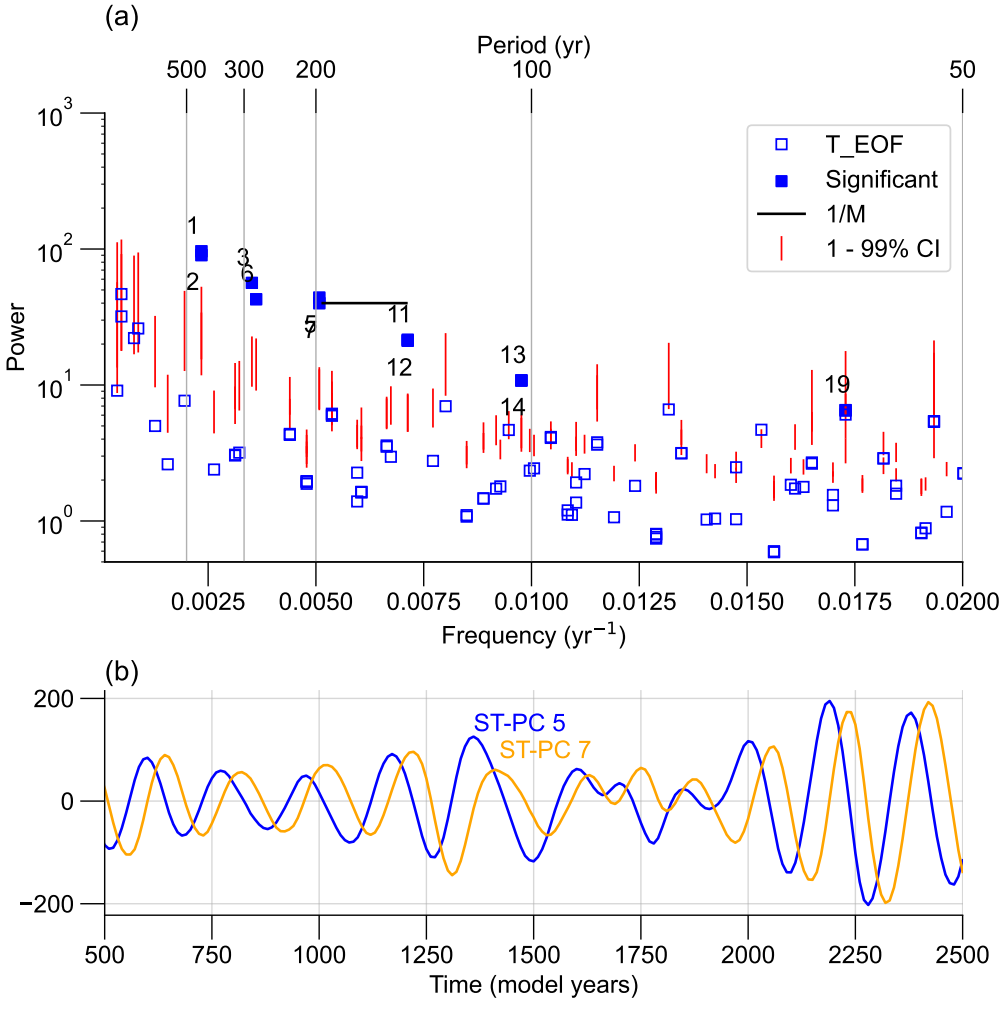


**Figure 4.** a) MSSA spectrum for the joint zonally averaged temperature and salinity fields with $M$ = 500 yr. T-EOFs are plotted at their associated frequency versus their eigenvalues, which indicate power. Red-lines show the 1-99% confidence intervals from the red-noise based significance test. Significant T-EOFs are indicated by filled markers, where the numbers indicate the corresponding T-EOF. The horizontal black line indicates the distance $1/M$ in frequency space (Sect. 2.2.3). If T-EOF pairs are separated by $1/M$ they cannot be considered as separate modes. Panel a) shows 5 pairs of significant T-EOF of the same frequency, where only T-EOF pair 3-6 does not have the same power. b) Temporal evolution of the ST-PCs associated with the T-EOF pair 5-7 with a periodicity of 200-yr. When one of the ST-PCs (or T-EOFs) leads the other by a quarter phase, the pair is considered to be in quadrature. Panel b) shows this is the case for ST-PC pair 5-7, which therefore meets the quadrature criterium (Sect. 2.2.2).

https://doi.org/10.5194/egusphere-2026-2794
Preprint. Discussion started: 11 June 2026
© Author(s) 2026. CC BY 4.0 License.

To determine the robustness of the potential modes we repeat the analysis with window sizes $M$ of 400, 600, 700, and 800 yr and summarise the results in Fig. 5a. The 200 and 140-yr modes are consistently present across the different window sizes and always meet the frequency and quadrature criteria. The 140-yr mode also meets the power criterium in 4 out of 5 window sizes, while the 200-yr mode never meets the power criterium. However, visual inspection of the MSSA spectrum for $M$ = 500 yr (Fig. 4a) suggests the T-EOF pair associated with the 200-yr mode are of nearly equal power. This suggests the automated method to determine the power criterium (Sect. 2.2.3) may be too strict. There is evidence of a potential higher frequency mode (105 yr) in 3 out of 5 window sizes, where at least the frequency and quadrature criteria are met. There is some evidence of lower frequency modes (280, 340, 440 yr), but these modes only meet the frequency and quadrature criteria in 1 or 2 out of the 5 window sizes. We also analyse the zonally averaged temperature and salinity fields separately. MSSA applied only to the zonally averaged salinity field shows evidence of a 280, 200, and 140-yr mode that meet the frequency and quadrature criteria for at least 4 out of 5 window sizes (Fig. A1a). MSSA applied only to the zonally averaged temperature field shows evidence of a 200, 140, and 105-yr mode that meet the frequency and quadrature criteria for at least 4 out of 5 window sizes (Fig. A1b). Additionally, the 280-yr mode is present for 3 out of 5 window sizes and meets the frequency and quadrature criteria.

In short, the 200 and 140-yr modes are consistent features in the zonally averaged salinity, zonally averaged temperature, and joint zonally averaged salinity and temperature MSSA spectra across different window sizes. Both modes consistently meet the frequency and quadrature criteria, and the 140-yr mode generally also meets the power criterium. The periodicities of the modes also align with local peaks in the multi-taper power spectrum of the AMOC time-series (Fig. 3b). Therefore, we consider both the 200 and 140-yr modes as robust modes of variability, where the 140-yr mode is most robust, as it generally also meets the power criterium. The 280-yr mode is sensitive to the window size parameter but there is evidence of the mode in the zonally averaged salinity, zonally averaged temperature, and joint zonally averaged salinity + temperature MSSA spectra. The sensitivity to the window size limits the robustness of this mode, but we consider it likely the mode is a feature of mCAV as it has a haline and thermal component and aligns well with the lower frequency variability in the power spectra (Fig. 3b,c).

While there is evidence of a potential 105-yr mode in the zonally averaged temperature and joint zonally averaged salinity and temperature MSSA spectra, the mode is identified in only 1 out of 5 window sizes in the zonally averaged salinity spectra (Fig. A1a). We do not consider this as a robust mode of mCAV, as such a mode is expected to be present in both the temperature and salinity fields. The MSSA results show some evidence of lower-frequency modes associated with periods of 340 and 440 yr and these periodicities aligns well with the multi-taper and wavelet power spectra (Figs. 3b,c). However, these modes are inconsistent across different window sizes and there is no evidence of these modes in the zonally averaged temperature analyses (Fig. A1b). Consequently, we do not consider these lower-frequency modes as robust features of mCAV. We did not investigate potential modes associated with (multi-)decadal frequencies as the focus is on (multi)-centennial variability.

A key strength of MSSA is the possibility to reconstruct the filtered spatio-temporal patterns associated with the identified modes (Sect. 2.2.1, 2.2.2). We reconstruct the spatio-temporal pattern from MSSA for a window size $M$ = 500 yr and focus on the 140-yr mode as it is most robust. Therefore, we select T-EOF pair 11-12 ($M$=500 yr, Fig. 5a) and compute ST-RC 11-12 for the zonally averaged temperature and salinity fields. Figure 5b shows the spatio-temporal temperature evolution of approximately half a cycle of the 140-yr mode in 20-yr intervals.

https://doi.org/10.5194/egusphere-2026-2794
Preprint. Discussion started: 11 June 2026
© Author(s) 2026. CC BY 4.0 License.

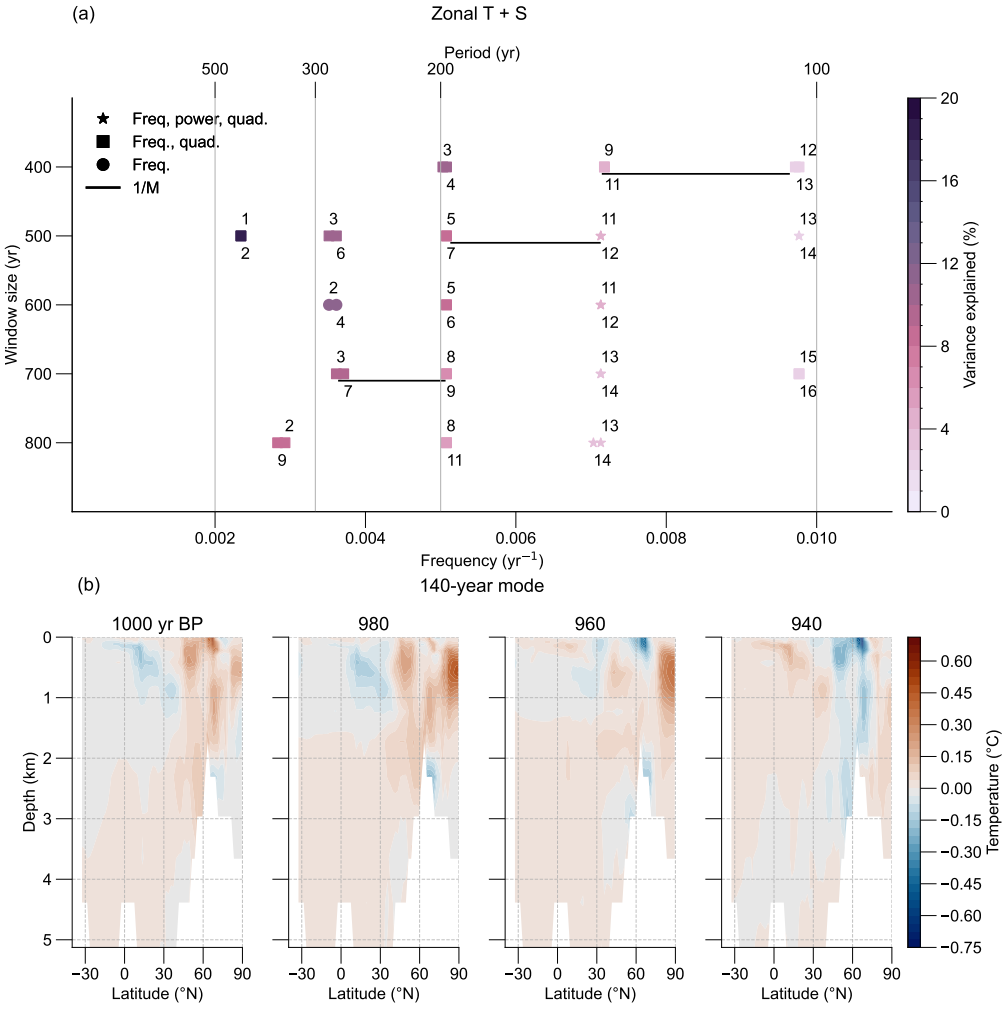


**Figure 5.** a) Overview of the MSSA spectra for the joint zonally averaged temperature and salinity fields for varying window sizes. For a given window-size $M$ (y-axis), the significant eigenvector pairs that have the same frequency are extracted from the MSSA Spectra. Markers indicate which oscillation criteria are satisfied by the eigenvector pairs. The marker colour indicates the percentage of variance explained by the eigenvector pair. Horizontal black lines indicates the distance $1/M$ in frequency-space. E.g., The MSSA spectra of Fig. 4a is summarised in panel a) at $M$=500 yr. b) Spatio-temporal evolution of temperature anomalies associated with the 140-yr mode over 20-yr intervals. The 140-yr mode is based on ST-RC pair 11-12, retrieved from the joint zonally averaged salinity and temperature analysis ($M = 500$, panel a).

https://doi.org/10.5194/egusphere-2026-2794
Preprint. Discussion started: 11 June 2026
© Author(s) 2026. CC BY 4.0 License.

The strongest temperature signal (up to ∼0.5°C) is in the Arctic north of 80°N. At 1000 yr BP, there is a warm anomaly above ∼1500 m sitting on top of a weaker, cold anomaly. Over the next 40 yr, the warm anomaly intensifies and deepens. Meanwhile, the cold anomaly aggregates at 2500 m depth around 70° N (980 BP), and potentially moves along the overflow pathways over the Greenland-Scotland ridge (960 BP). After 60 yr, the initial state is approximately reversed with a cold anomaly in the upper 1000 m north of 80°N and warm anomalies below. There is also a clear temperature signal around the deep water formation latitudes 50-70°N. At 1000 yr BP the warm anomalies are spread throughout the water column. During the next 40 yr the warm anomalies at a depth of 1.5-3 km propagate southward. The propagation of anomalies in the lower AMOC limb suggests these modes are associated with the AMOC. By 940 yr BP, the initial state is reversed with cold anomalies dominating the water column around 60°N. A final region of interest is the (sub)tropical North Atlantic between 100-1500 m depth, where a cold anomaly aggregates between 1000 and 980 yr BP. By 960 BP, the cold anomaly has breached the surface around 30°N and weakened. At the same time, a strong cold anomaly has formed in the upper 500 m layer around 60°N. It is unclear if this cold anomaly is associated with an advective process from the subtropical subsurface, from the Arctic, or from other processes such as surface ocean-atmosphere interactions. By 940 BP, a warm temperature anomaly has formed in the subtropical subsurface, reversing the phase of the oscillation. The spatio-temporal behaviour of the 200-yr mode is very similar to the 140-yr mode (Fig. A4a). There are small differences, with the 200-yr mode showing a more uniform pattern in the Arctic and the (sub)tropical subsurface anomalies extending more clearly to the South Atlantic (sub)tropics.

### 3.3 Modes of AMOC variability: surface and upper ocean perspective

While the zonally averaged temperature and salinity fields are useful to identify the modes of AMOC variability, marine proxy reconstructions typically better reflect surface or upper ocean temperatures. Therefore, we also apply MSSA to the SST and the upper ocean temperature fields, here defined as the average temperature taken over the upper 300 metres. Additionally, we apply MSSA separately to the salinity fields and in a joint MSSA with temperature to test the robustness of the modes.

The MSSA spectra for the upper ocean temperature analyses show potential modes with periods of 200, 140, and 105 yr that meet the frequency and quadrature criteria for all window sizes Fig. (6a). Similar to the zonally averaged analysis, the 140-yr mode also consistently meets the power criterium. There is also evidence of a 280 and 440-yr mode for 3 out of 5 window sizes where the frequency and quadrature criteria are met. Including both upper ocean temperature and salinity fields into a joint MSSA leads to robust identification of the 280, 200, 140, and 105-yr modes (Fig. A2a). However, when only the upper ocean salinity field is considered, the 280, 140, and 105-yr modes are less robust (Fig. A2b).

We also perform the analyses for the SST and SSS fields to determine if the results are sensitive to the definition of the latitude-longitude field. The 280, 200, and 140-yr modes are robust features of the SSS, SST, and joint SSS + SST MSSA spectra (Fig. A3). The joint SSS + SST spectra also consistently show evidence of the 105-yr mode, but this mode is only present in 1 out of 5 window sizes for the SST spectra. Similarly, the SSS spectra show evidence of a 340-yr mode in 4 out of 5 window sizes (Fig. A3b), but the mode is not present for any window size in the SST spectra (Fig. A3c).

The spatio-temporal evolution of the 140-yr mode is characterised by upper ocean temperature anomalies (∼1°C) in the subpolar North Atlantic, Greenland, Iceland, and Norwegian (GIN) Seas, and the Arctic Ocean, particularly the Barents Sea

https://doi.org/10.5194/egusphere-2026-2794
Preprint. Discussion started: 11 June 2026
© Author(s) 2026. CC BY 4.0 License.

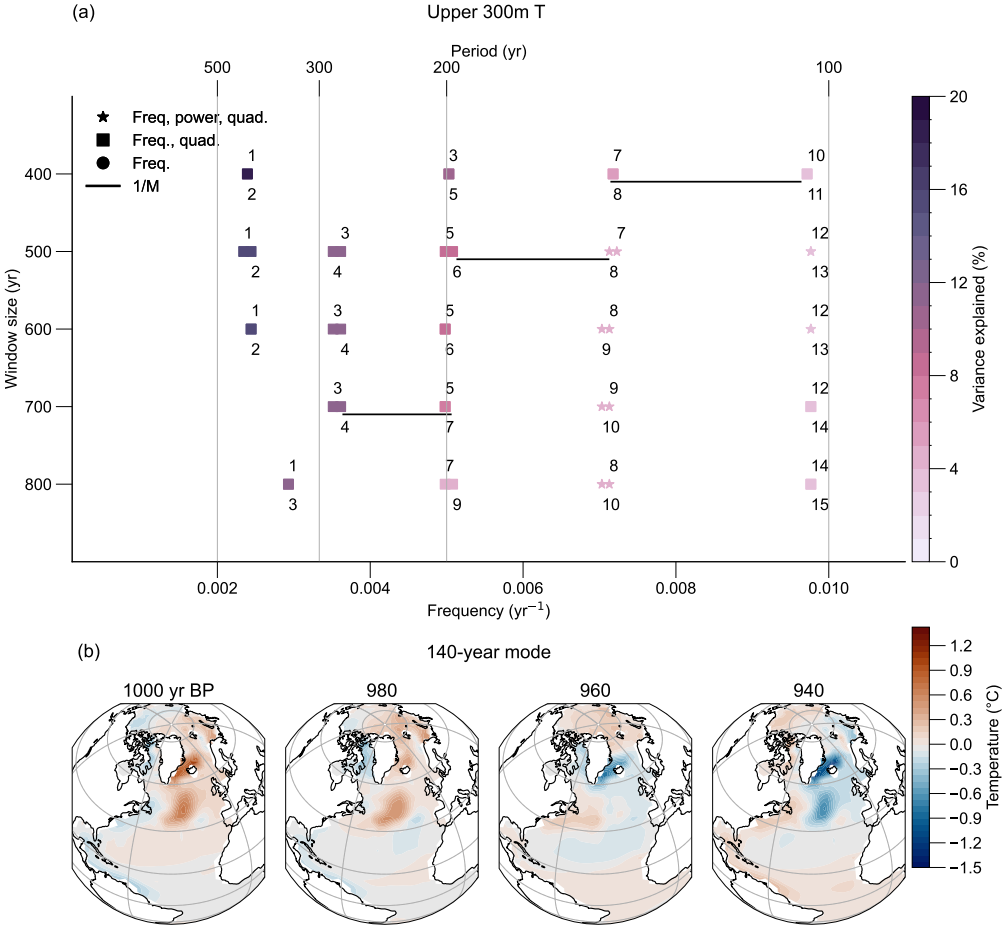


**Figure 6.** a) Overview of the MSSA spectra for the upper 300 m ocean temperature field for varying window sizes. Figure as in Fig. 5a. b) Spatio-temporal evolution of temperature anomalies associated with the 140-yr mode over 20-yr intervals. The 140-yr mode is based on ST-RC pair 7-8 retrieved from the upper ocean temperature analysis ($M$ = 500 yr, panel a).

https://doi.org/10.5194/egusphere-2026-2794
Preprint. Discussion started: 11 June 2026
© Author(s) 2026. CC BY 4.0 License.

(Fig. 6b). Anomalies in the subpolar North Atlantic and the GIN seas show stationary behaviour, while anomalies in the Arctic show propagative behaviour. At 1000 yr BP, there are warm temperature anomalies in the Barents Sea, which spread eastward towards the Beaufort Sea and Baffin Bay during the next 60 yr. By 940 yr BP, there are cold anomalies in the Barents Sea and the reverse phase of the oscillation begins. A notable feature of the mode is the horseshoe-like pattern at 960 yr BP with warm anomalies in the subpolar North Atlantic, flanked by cold anomalies in the north, east, and south, often associated with Atlantic Multidecadal Variability (Kushnir, 1994). South of 30°N, the temperature anomalies associated with the mode are smaller, though distinct and often opposing anomalies can be identified in the Gulf Stream region and the subtropical gyre. The spatio-temporal behaviour of the 200-yr mode is qualitatively similar to that of the 140-yr mode (Fig. A4b). The spatio-temporal patterns in the 200 and 140-yr modes of the SSTs are largely similar to those of the upper ocean temperatures, though there are two key differences (Fig. A6). Compared to the upper ocean temperature modes, the SST modes show anomalies in the Barents Sea that are of opposite sign and there is no indication that the Barents Sea SST anomalies propagate around the Arctic. Additionally, south of 30°N, there is no clear SST signal in the Gulf Stream region, while there is a signal in this region in the upper ocean temperature modes (Fig. 6b).

### 3.4 Modes of AMOC variability: Proxy Grid

Thus far, we have used input data for MSSA that covers the Arctic and Atlantic Ocean in the latitude-longitude or latitude-depth space, reflecting data in the order of $\sim 10^3$ degrees of freedom. We have shown two key strengths of MSSA, namely the ability to identify modes of variability from a set of geo-spatial time series, and the ability to reconstruct the spatio-temporal patterns associated with the identified modes. However, data availability is among the main limiting factors when researching past climates and it is unclear how this affects MSSA performance. Therefore, it is interesting to explore if the strengths of MSSA are retained when the input data more realistically reflects the degrees of freedom of geological proxy reconstructions. We again apply MSSA to the upper ocean temperatures, but now include only cells of the Proxy Grid (Sect. 2.1.2), which contains just 35 ocean grid-cells (Fig. 1). We apply MSSA to the input data constrained by the Proxy Grid and explore the ability of MSSA to identify the three most robust modes (280, 200, 140-yr) identified in analyses of Sect. 3.2, and 3.3. We may also expect to find evidence of the less robust 440 and 105-yr modes, which are features of the Full Grid upper ocean temperature MSSA results (Fig. 6a). Salinity fields are not included in the analysis as salinity proxy reconstructions are very rare.

The Proxy Grid upper ocean temperature MSSA results are summarised in Fig. 7a. There is evidence of a 140-yr mode that meets at least the frequency and quadrature criteria in 3 out of 5 window sizes. There is also evidence of a 280-yr mode in 3 out of 5 window sizes, though one of the oscillatory pairs does not meet the quadrature criterium. There is no evidence of T-EOF pairs associated with the 200-yr mode. Compared to the Full Grid analyses, the Proxy Grid MSSA evidence of the 280 and 140-yr modes is less robust and the 200-yr mode is not identified at all. This may suggest the signal-to-noise ratio in the Proxy Grid is too low to robustly identify the modes that are present in the upper ocean temperature fields. Nonetheless, the evidence of the 280, and 140-yr modes suggest mCAV is present within the data constrained by the Proxy Grid.

https://doi.org/10.5194/egusphere-2026-2794
Preprint. Discussion started: 11 June 2026
© Author(s) 2026. CC BY 4.0 License.

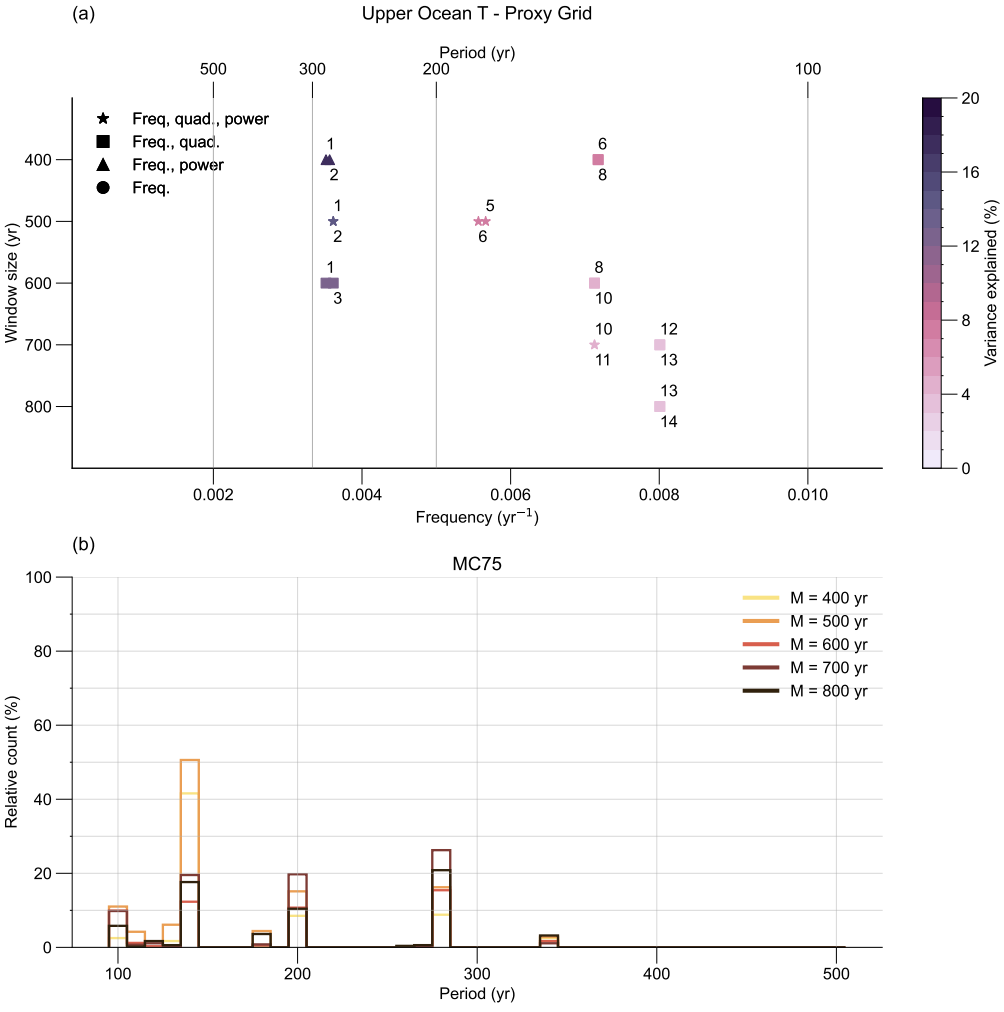


**Figure 7.** a) Overview of the MSSA spectra for the upper 300 m ocean temperature field when the input data is constrained by the Proxy Grid. Figure as in Fig. 5a. b) Relative frequency histograms that summarise the results of the MC75 experiment. Colours indicate different window sizes. The histograms indicate the percentage of MC realisations where an oscillatory mode is identified at a given period (x-axis). To be considered as an oscillatory mode a T-EOF pair must be significant and satisfy the frequency, quadrature, and power criteria.

In an attempt to extract the signal from the noise, we increase the parameter space of the problem by applying MSSA to many different combinations of grid cells that are part of the Proxy Grid. Specifically, we further subsample the Proxy Grid and randomly select 75% of the grid cells (26 out of 35) and apply MSSA with a red-noise surrogate test based on 100 realisations. From the MSSA spectrum, we store eigenvalue pairs that exceed the 99$^{\text{th}}$ percentile of the surrogate test and meet the oscillatory criteria of frequency, quadrature, and power. For each window size ($M$ = 400, 500, 600, 700, 800 yr), we repeat this process 1000 times in a Monte Carlo approach and refer to this experiment as MC75. We summarise the results by creating relative frequency histograms that indicate how often a mode is identified within the 1000 realisations (Fig. 7b).

https://doi.org/10.5194/egusphere-2026-2794
Preprint. Discussion started: 11 June 2026
© Author(s) 2026. CC BY 4.0 License.

In the MC75 experiment there are five potential modes that are identified across the different window sizes. The 280, 200, and 140-yr modes are the three most commonly identified modes independent of window size. These modes align with the three most robust modes of mCAV identified in the analyses on the zonally averaged salinity and temperature fields (Sect. 3.2). The identification rate of the 140-yr mode is between ∼12-50%, while identification rates of the 280 and 200-yr modes have upper bounds of ∼25% and 20% respectively, and similar lower bounds of ∼10%. The fourth most commonly identified mode falls in the 95-105-yr bin with identification rates between the ∼3-11%. This mode reflects the ∼105-yr mode that is also present in the Full Grid upper ocean temperature analysis (Fig. 6a). There is some evidence of a potential 340-yr mode, though the mode has very low identification rates (∼2-4%). This potential 340-yr mode is not a common feature of the Full Grid analysis on temperature fields, but is a robust feature of the Full Grid SSS field (Fig. A3b) and the upper ocean salinity field (Fig. A2b).

In the literature, the power criterium is sometimes relaxed or not applied (e.g., Manta et al., 2024; Seitola et al., 2015). Furthermore, the heuristic implementation of the power criterium in this study may be too strict (3.2). Therefore, we perform an additional sensitivity experiment where only the frequency and quadrature criteria are applied. The same 280, 200, and 140-yr modes are most commonly identified, but at higher identification rates (∼22-72%) (Fig. A10a). However, in the sensitivity experiment there is also more evidence of non-robust modes associated with periods of 120, 180, and 340-yr. Next, we further constrain the input data and repeat the Monte Carlo Proxy Grid subsampling experiment by randomly subsampling 50% (MC50, 17 grid-cells) and 25% (MC25, 8 grid-cells) of the Proxy Grid. Both the MC50 and MC25 experiment lead to the same conclusion as MC75, where the 280, 200, and 140-yr modes are the three most commonly identified modes independent of window size (Fig. A10b,c). While the identification rate of the 200-yr mode is relatively insensitive to the amount of input data, the 280 and 140-yr modes are affected. The upper bounds of the identification rate of the 140-yr mode decrease from ∼52% (MC75) to ∼23% (MC25), largely due to a decrease in the identification rate in window sizes $M$ = 400 and 500 yr. The 280-yr mode is affected in the opposite way, with the upper bound increasing from ∼25% (MC75) to ∼37%, largely due to an increase in the identification rate in window sizes $M$=700 and 800 yr.

### 3.5 Spatio-temporal coherence

The Monte Carlo Proxy Grid subsampling procedure shows MSSA remains a powerful way to determine modes of variability when input data is realistically constrained. In this section, we explore if MSSA retains its second strength of reconstructing filtered spatio-temporal patterns related to the modes when the input data is constrained. More specifically, we determine if the modes identified from the MC Proxy Grid experiments are coherent in space and time compared to the modes identified from the Full Grid.

We use the filtered spatio-temporal upper ocean temperature anomalies related to the 140-yr mode from the Full Grid analysis (Fig. 6b) to compute time-series over the sectors indicated in Fig. 1. Next, we determine the phase relationship with respect to the Irminger sector. Specifically, we retain the phase lead associated with the maximum correlation coefficient within the range of $[0, T_{av}]$, where $T_{av}$ represents the dominant period of the mode. We compare with respect to the Irminger sector as it contains the most proxy locations, which likely makes the sector the least sensitive to subsampling. We repeat this process

https://doi.org/10.5194/egusphere-2026-2794
Preprint. Discussion started: 11 June 2026
© Author(s) 2026. CC BY 4.0 License.

for each of the realisations of the MC Proxy Grid ensembles ($M = 500$ yr) that finds a significant 140-yr mode that meets the frequency, quadrature, and power criteria. We use the distribution of phase leads of the MC Proxy Grid ensembles to construct the histograms in Fig. 8. We describe the spatio-temporal coherence between the 140-yr mode of the Full Grid and the MC experiments with a measures of accuracy and precision. The measures are based on the mean and standard deviation of the distribution of phase leads associated with a specific region and MC experiment. Accuracy is indicated by the distance between the Full Grid phase lead and the MC experiment mean phase lead ($\text{mean}_\theta$). Precision is indicated by the phase lead standard deviation ($\text{std}_\theta$). We calculate the mean and standard deviation based on circular statistics (Mardia and Jupp, 1999) because we are analysing oscillatory modes.

To exemplify the spatio-temporal signals in the MC-Proxy Grid ensembles, Fig. 8 shows the two sectors where the signals are most coherent and (among the) least coherent. For the Full Grid 140-yr mode, the southern GIN (S-GIN) sector is in phase (0 yr lead) with the Irminger sector, as indicated by the orange line in Fig. 8a. We consider this 0 yr phase lead as baseline and use it as comparison for the phase leads of the 140-yr modes identified in the MC Proxy Grid ensembles. For each realisation of the MC75 ensemble that contains a 140-yr mode, nearly 100% show the same in phase relationship between the S-GIN and Irminger sector (Fig. 8a). This results in a circular mean phase lead very close to the lead of the Full Grid, indicating high accuracy. Additionally, the spread of the MC75 ensemble is very small ($\text{std}_\theta \sim 1$ yr), indicating high precision. Further reducing the input data size to the MC50 and MC25 ensembles has a negligible effect on the accuracy, while the precision decreases slightly. Overall, reducing the input data size only has a small effect on the spatio-temporal coherence between the S-GIN and the Irminger sector. Other sectors with high accuracy and precision are the East North Atlantic, West North Atlantic, and northern GIN (N-GIN) (Fig. A7). In these sectors, decreasing the input data size to MC50 and MC25 also has a negligible effect on the accuracy while decreasing the precision.

The Full Grid ST-RCs associated with the 140-yr mode show the Beaufort sector leads the Irminger sector by 60 yr (Fig. 8b). The MC75 realisations with a 140-yr mode show a the Beaufort sector has a circular mean phase lead of ∼55 yr, making it reasonably accurate. However, only ∼20% of the realisations fall within the 60-yr lead bin, and there is a relatively large spread ($\text{std}_\theta \sim 11$ yr), highlighting the lower precision in the reconstructed spatio-temporal pattern. Further reducing the input data size to the MC50 and MC25 shifts the mean lead towards longer timescales and decreases the precision further. The Gulf of Mexico and Benguela are other sectors with a lower accuracy and lower precision (Fig. A7) compared to the regions in the North Atlantic.

We repeat the analysis of the spatio-temporal coherence for the 200 and 280-yr modes. Results for the 200-yr mode are largely similar compared to the 140-yr mode, with two exceptions (Fig. A8). In the 200-yr mode, the West North Atlantic region shows much lower accuracy and precision, and becomes the least coherent sector. Additionally, the Gulf of Mexico shows relatively higher accuracy and precision in the 200-yr mode.

Results for the 280-yr mode indicate the S-GIN and East North Atlantic remain among the modes with highest accuracy and precision (Fig. A9), similar to the 140-yr mode. The Gulf of Mexico, Benguela, and Beaufort sector also perform relatively well in terms of accuracy and precision, marking a clear difference with the 140-yr mode. In the 280-yr mode, the N-GIN and West North Atlantic show the lowest spatio-temporal coherence with low accuracy and precision.

https://doi.org/10.5194/egusphere-2026-2794
Preprint. Discussion started: 11 June 2026
© Author(s) 2026. CC BY 4.0 License.

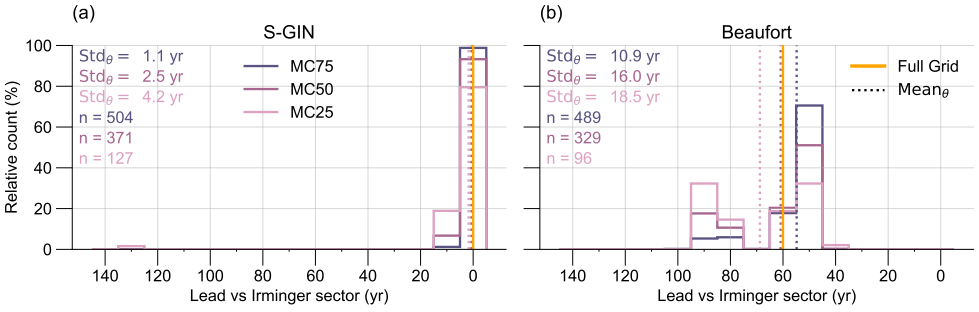


**Figure 8.** Spatio-temporal coherence of the 140-yr mode between the Full Grid (orange) and the MC experiments (shades of pink) for a window size $M$ = 500 yr. Panels show the phase lead of the time-series computed over a) the S-GIN sector, and b) the Beaufort sector, relative to the Irminger Sector. The phase lead of the Full Grid is indicated by the orange vertical line. The relative frequency histograms illustrate the distribution of the leads from the Monte Carlo Proxy Grid ensembles for each realisation that contains a 140-yr mode and contains grid cells in both the given sector and the Irminger sector. The circular mean phase leads (mean$_\theta$) for the MC experiments are indicated by the dashed vertical lines. The text insets show the number of realisations that are included in the histogram and statistics, as well as the circular standard deviation of the phase leads (std$_\theta$) for the MC experiments. Results for other sectors are shown in Fig. A7.

https://doi.org/10.5194/egusphere-2026-2794
Preprint. Discussion started: 11 June 2026
© Author(s) 2026. CC BY 4.0 License.

## 4 Discussion & Conclusions

We introduced the paleoclimate community to MSSA and showcased a conventional use case where we identified robust modes of simulated mCAV from unconstrained input data. Next, we used the perfect model perspective to explore the potential applicability of MSSA to geological reconstructions by constraining the simulated data by the location and amount of potentially available geological reconstructions relevant to mCAV. We successfully used MSSA to trace the most robust modes of variability under the applied constraints. In a final step, we showed that modes identified with MSSA can be coherent in space and time between modes identified from unconstrained and constrained input data, though the coherence appears to depend on the region.

### 4.1 Identification of modes

The MSSA spectra summarised in Fig. 7a,b indicate the identification of modes based on the constrained input data is strongly dependent on the combination of cells from the Proxy Grid that form the input data. Exploring different combinations of input data with a Monte Carlo procedure resulted in the identification of the 280, 200, 140, 105-yr modes, and potentially a 340-yr mode. The MC75, MC50, and MC25 experiments consistently showed the 280, 200, and 140-yr modes as the modes with the highest identification rates. This shows the Monte Carlo procedure can extract the modes of mCAV we consider as most robust based on the zonally averaged salinity and temperature analyses (Sect. 3.2). Furthermore, there was limited evidence of identification of non-robust modes, which increases our confidence in the Monte Carlo procedure. The non-robust modes are likely limited due to the conditions that potential T-EOF pairs must satisfy to be considered as modes, namely to be significant, meet the frequency, quadrature, and power criteria, as well as be present across the different window sizes (Sect. 3.4).

It is possible that the strongly reduced size of the input data makes the analysis more susceptible to noisy time-series that distort the signal. However, we were unable to identify any grid-cell in the Proxy Grid that was less likely than others to be included in a MC realisation where we identify at least one of the 280, 200, or 140-yr modes (not shown). Therefore, we deem it likely that the signal-to-noise ratio is lower in the Proxy Grid based input data compared to the Full Grid, which makes the identification of modes more sensitive to input data and analysis choices. Our results highlight the importance of varying parameters in the application of MSSA, such as the window size and potentially the input data, particularly when the signal-to-noise ratio becomes very small.

### 4.2 Spatio-temporal coherence of modes

When a mode of the same period is identified from both the unconstrained and the constrained input data, the spatio-temporal coherence between the modes is generally high in the N-GIN, S-GIN, and East North Atlantic (Sect. 3.5). Additionally, the Monte Carlo subsampling approach shows the precision of the spatio-temporal coherence decreases with decreasing amounts of input data. While hardly surprising, it highlights the importance of finding a balance between a low number of high quality reconstructions or a larger number of reconstructions of lower average quality (e.g., Christiansen and Ljungqvist, 2017; Jaume-Santero et al., 2020). The spatio-temporal coherence is generally lower for regions that are located further away from the North

https://doi.org/10.5194/egusphere-2026-2794
Preprint. Discussion started: 11 June 2026
© Author(s) 2026. CC BY 4.0 License.

Atlantic, such as the Benguela and Beaufort regions. Coincidentally, the Beaufort and Benguela regions are also amongst the regions with the least grid cells in the Proxy Grid, which could negatively impact the spatio-temporal coherence because the anomalies cannot be averaged over multiple grid-cells. However, in the MC25 experiment all regions are statistically likely to contain just 1 or 2 grid cells and the Beaufort and Benguela region have among the lowest coherence in the MC25 experiment of the 140-yr mode (Fig. 8b, A7). Consequently, the amount of proxy-grid cells per region is not likely to be the dominant explaining factor for the low coherence. Alternative explanations for the lower coherence may be that these regions are not linked directly to AMOC dynamics, may be influenced by other local processes, or the centennial timescales may be too short for advective signals to emerge (e.g., Bakker et al., 2026). Indeed, the relative spatio-temporal coherence of the Benguela and Beaufort region compared to the other regions is higher for the 280-yr mode compared to the 140-yr mode.

A notable region is the West North Atlantic, which showed high precision for the 140-yr mode, but the lowest precision for the 200 and 280-yr modes (Figs. A7, A8, A9). This suggests the boundaries of the West North Atlantic as defined in this study (Fig. 1) may be unsuitable for extracting spatio-temporally coherent signals. The proxy reconstructions in the West North Atlantic region are located in an area that is influenced by the warm Gulf Stream and cold Labrador Current. The spatio-temporal behaviour of the 200 and 280-yr modes is much more heterogeneous in this region compared to the 140-yr mode (i.e., compare Figs. 6b and A4b, A5b), which may be related to these currents. However, the interactions between the Gulf Stream and Labrador Current are poorly represented by *i*LOVECLIM due to the low resolution and the exclusion of Newfoundland as a land mass in the ocean grid. Consequently, it is unlikely that our assessment of the spatio-temporal coherence in this region is accurate. Potentially, the spatio-temporal coherence could be improved by splitting the West North Atlantic sector into regions that are dominantly affected by either the Gulf Stream or the Labrador Current.

### 4.3 Potential effects of proxy uncertainties

Our research is limited by the methodological choice not to consider the variety of uncertainties that are associated with geological proxy reconstructions. In the context of mCAV, the climate signal may be relatively weak compared to analytical and calibration uncertainties, which may hinder the identification of multi-centennial modes with MSSA. In a first order estimate, Bakker et al. (2026) have shown the SST signal associated with 100-200 yr AMOC variability may only be detectable relative to analytical and calibration uncertainties in the region around Iceland and in a part of the subpolar gyre. However, this estimate assumes a mCAV amplitude of 8% (relative to the mean AMOC strength) based on previous mCAV model studies. As climate models typically underestimate regional climate variability on (multi-)centennial timescales (Lovejoy et al., 2013; Ellerhoff and Rehfeld, 2021; Zhu et al., 2019; Hébert et al., 2022; Laepple et al., 2023), the 8% estimate could very well be an underestimation compared to the real climate system. Bioturbation could further distort the multi-centennial signal by smoothing the signal (Berger and Heath, 1968; Hutson, 1980; Löwemark, 2025).

Age uncertainties associated with marine sedimentary archives form another potential obstacle in detecting modes of variability. In Holocene marine sediments, age uncertainties associated with carbon dating are typically in the range of several decades (Anchukaitis and Tierney, 2013). Bioturbation can also influence age uncertainty related to the age-heterogeneity of the sediment (Andree, 1987; Lougheed et al., 2020; Löwemark, 2025). Age uncertainties could also negatively impact the

https://doi.org/10.5194/egusphere-2026-2794
Preprint. Discussion started: 11 June 2026
© Author(s) 2026. CC BY 4.0 License.

spatio-temporal coherence of identified modes. Consequently, it is essential that age uncertainties are included in any analysis on phase relationships between different marine sediment proxy reconstructions (Franke and Donner, 2019; Anchukaitis and Tierney, 2013). MSSA requires further development to include proxy-uncertainties but MSSA is readily applicable to archives with high temporal resolution and less influenced by age uncertainties, such as records from tree rings. Indeed, Taricco et al. (2015) applied MSSA to 26 (17) mostly annually resolved Northern Hemisphere extratropical temperature reconstructions that cover the last millennium (last two millennia). They found multi-decadal and (multi-)centennial modes and were able to infer propagative behaviour between latitude belts. It is plausible that the modes identified by Taricco et al. (2015) are related to AMOC variability because the identified signal was particularly high around the North Atlantic and terrestrial variability on these timescales is typically ocean-driven (Hébert et al., 2022).

### 4.4 *i*LOVECLIM mCAV

We identified robust 280, 200, and 140-yr modes of mCAV in the Late Holocene *i*LOVECLIM simulation (3.2). The modes display very similar spatio-temporal patterns, where the temperature signal is strongest in the Arctic Ocean and the subpolar North Atlantic (Figs. 5b, 6b, A4, A5). This suggests the *i*LOVECLIM mCAV mechanism may be similar across the modes and can act on different timescales. Other modelling studies have suggested the mCAV in their simulations is driven by processes in the Arctic (Jiang et al., 2021; Meccia et al., 2023; Mehling et al., 2023; Mehling, 2024) or subpolar North Atlantic (Yang et al., 2024b; Cao et al., 2023). As these regions show a strong signal in our analysis these processes could also play a role in the *i*LOVECLIM simulation.

In several of the MSSA spectra we found evidence of potential lower frequency modes with periodicities of 340 yr (e.g., Figs. A2b, A3b) or 440-yr (Fig. 6a). These potential modes align well with the spectral analysis of the AMOC (Fig. 3b,c), which suggests these modes may be relevant features of the mCAV in the simulation. It is possible that the strongly quasi-oscillatory low frequency variability becomes aliased into different low-frequency eigenvectors depending on exact MSSA configuration (e.g., Taricco et al., 2015). However, this is speculative and these low-frequency modes cannot be considered robust due to their sensitivity to window size and/or dominant presence in either the temperature or salinity fields. Nonetheless, we showed that the AMOC strength in the simulation is characterised by a broad multi-centennial spectrum (Fig. 3b) and multiple distinct modes. Several modern ESMs (e.g., CanESM5, IPSL-CM6A-LR, EC-Earth3, and UKESM1-0-LL) also show multi-taper spectra of AMOC time-series with a broad multi-centennial power spectrum (Mehling et al., 2024). Our results imply that the mCAV in these models may also be characterised by several distinct modes, which has thus far typically not been considered in mCAV research.

### 4.5 Outlook

In this study we showed it is possible to identify robust modes of simulated (multi-)centennial AMOC variability under strongly constrained input data that more realistically reflects the geological record in terms of location and number of records. Furthermore, we showed that the modes identified based on the constrained input data generally retain their spatio-temporal coherence within the northern and eastern North Atlantic. These findings suggest MSSA can be a suitable tool to extract modes of variabil-

https://doi.org/10.5194/egusphere-2026-2794
Preprint. Discussion started: 11 June 2026
© Author(s) 2026. CC BY 4.0 License.

ity and associated spatio-temporal patterns from geological reconstructions. Consequently, we believe MSSA can function as the key methodology in the Mechanistic Indicators framework to construct hypotheses of mechanisms of mCAV in models and to use the geological record to falsify such hypotheses. This motivates further work that incorporates uncertainties associated with geological reconstructions into the MSSA methodology, which is a necessary step if phase-relationships are inferred from geological reconstructions (Franke and Donner, 2019; Anchukaitis and Tierney, 2013). From the dynamical oceanography perspective, the Mechanistic Indicators framework motivates the identification and clustering of phase relationships in different models that may contain different mechanisms of mCAV. In this context, our results highlight the importance of considering the possibility that a broad multi-centennial AMOC spectrum can contain multiple distinct modes of variability that could be related to different mechanisms. Furthermore, even though salinity anomalies typically play a dominant role in mechanisms of mCAV (e.g., Jiang et al., 2021; Yang et al., 2024b; Meccia et al., 2023; Mehling et al., 2024), we highlight it is critical to include temperature fields in the study of mechanisms of mCAV as evidence of phase relationships from the geological record necessarily depends on temperature, and not salinity, reconstructions.

https://doi.org/10.5194/egusphere-2026-2794
Preprint. Discussion started: 11 June 2026
© Author(s) 2026. CC BY 4.0 License.

*Code and data availability.* The *i*LOVECLIM output and the processed data required to create figures are available through Zenodo 10.5281/zenodo.20122669 (Bense, 2026a). The notebooks to create the figures are available at https://github.com/tbense/Bense_ea_2026_Extracting_coherent_spatio and archived through Zenodo 10.5281/zenodo.20201057 (Bense, 2026b). The HadISST dataset is available through NSF NCAR GDEX https://doi.org/10.5065/XMYE-AN84 (Hadley Centre for Climate Prediction and Research//Ministry of Defence/United Kingdom and Office, 2000). The temperature 12k database (Kaufman et al., 2020) is available through WDS-NOAA https://doi.org/10.25921/4ry2-g808. The PAGES 2k temperature database (PAGES2k Consortium et al., 2017) is also available through WDS-NOAA https://doi.org/10.25921/ycr3-7588.

The MSSA analysis is largely based on an adjusted version of the mssakit python package by Saraswati and de Viron (2023) (https://github.com/anitasaraswati/MSSAkit/). The MTM analysis was performed using code from Mehling (2024) (https://github.com/omehling/centennial-variability-CMIP6). The wavelet analysis was performed using the PyCWT package from Krieger and Freij (2025)(https://github.com/regeirk/pycwt). Linear colour maps are based on Crameri et al. (2020) and can be obtained through Zenodo 10.5281/zenodo.1243862.

https://doi.org/10.5194/egusphere-2026-2794
Preprint. Discussion started: 11 June 2026
© Author(s) 2026. CC BY 4.0 License.

## Appendix A

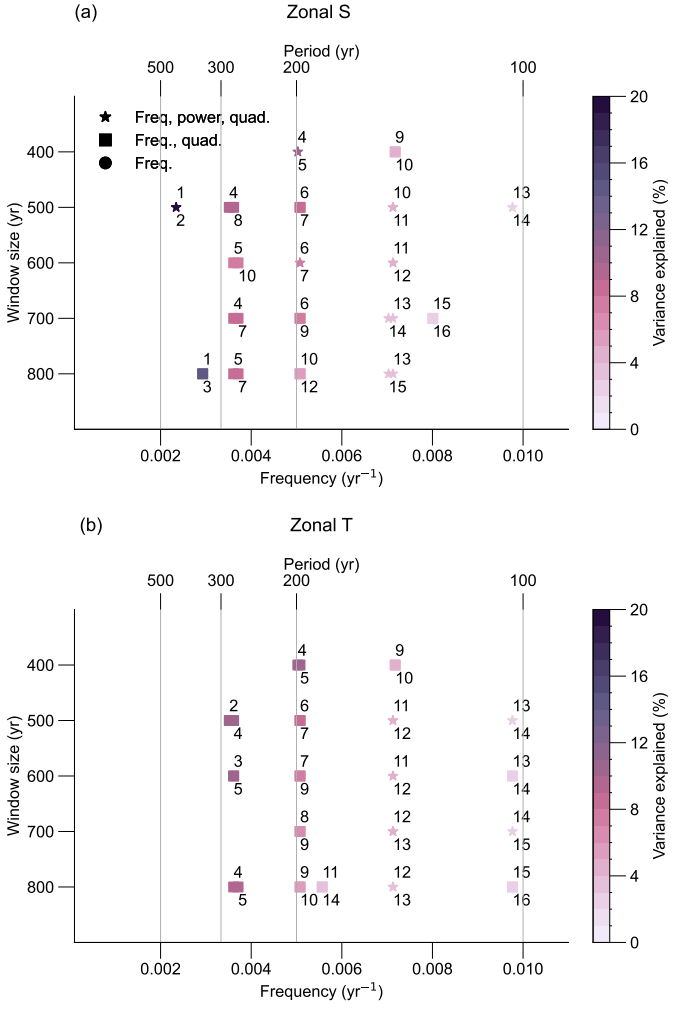


**Figure A1.** Overview of the MSSA spectra for a) the zonally averaged salinity field, and b) the zonally averaged temperature field. Figure as in Fig. 3a.

https://doi.org/10.5194/egusphere-2026-2794
Preprint. Discussion started: 11 June 2026
© Author(s) 2026. CC BY 4.0 License.

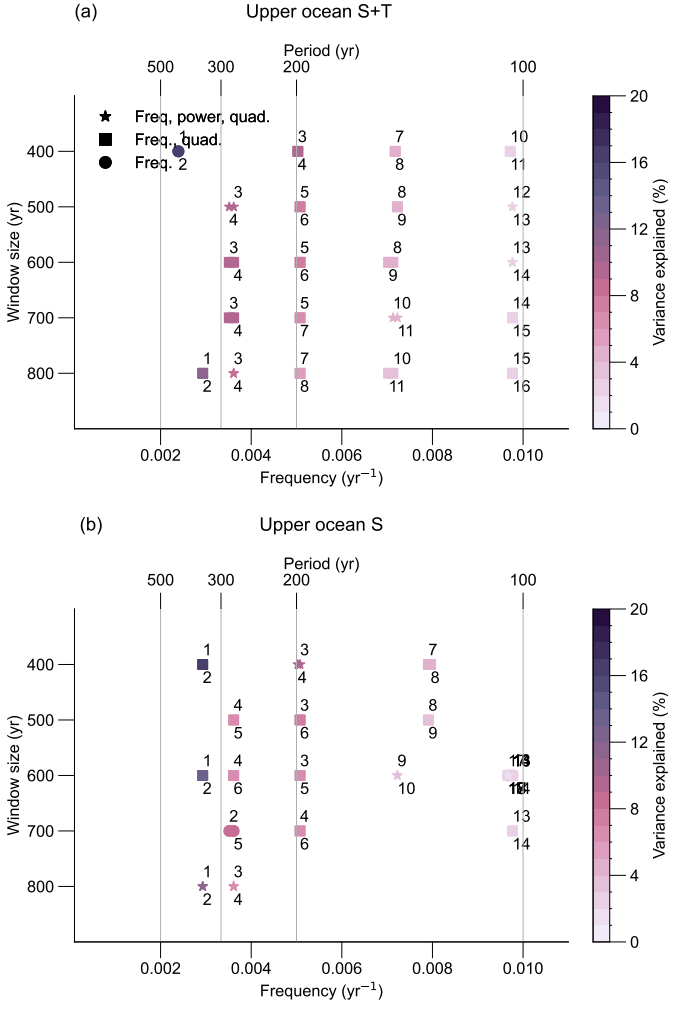


**Figure A2.** Overview of the MSSA spectra for a) the joint upper 300 m ocean salinity and temperature fields, and b) the upper 300 m ocean salinity field. Figure as in Fig. 3a.

https://doi.org/10.5194/egusphere-2026-2794
Preprint. Discussion started: 11 June 2026
© Author(s) 2026. CC BY 4.0 License.

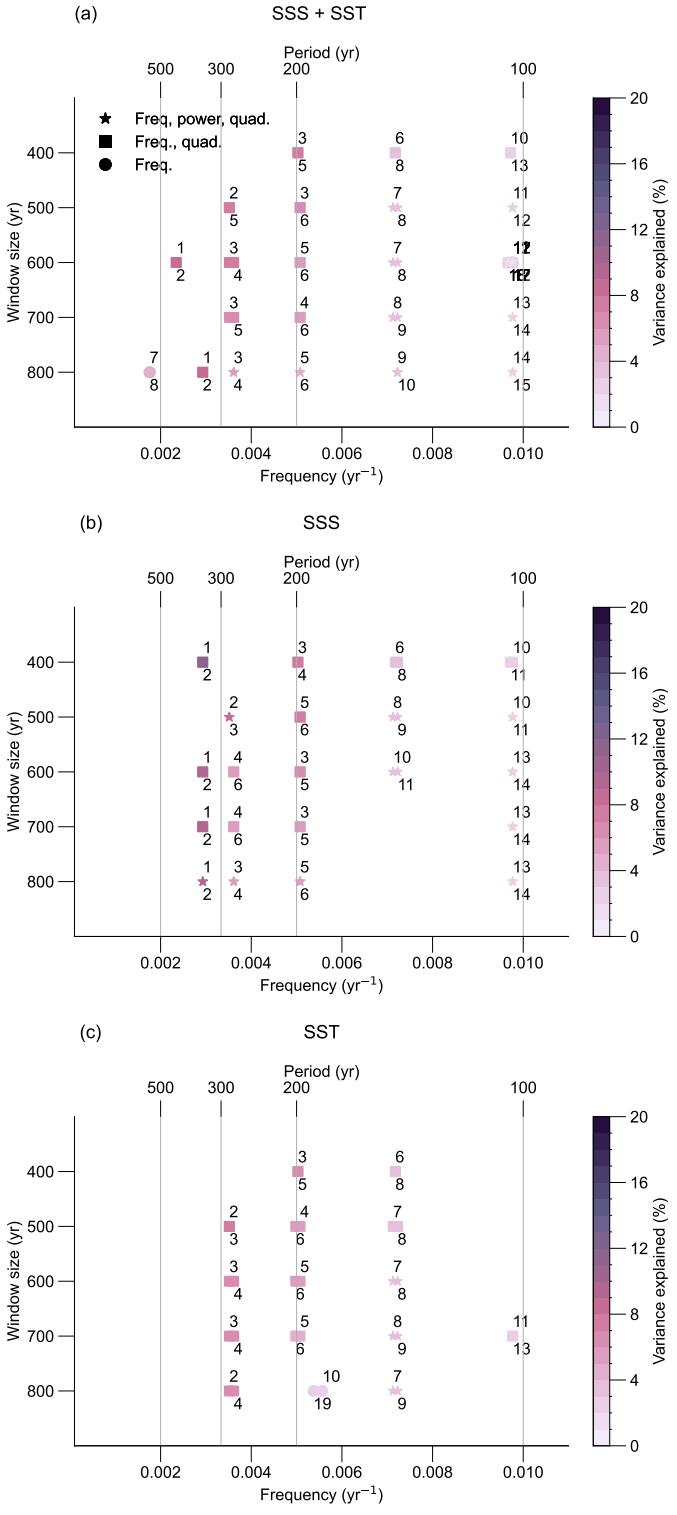


**Figure A3.** Overview of the MSSA spectra for a) the joint SSS and SST fields, b) the SSS field, and c) the SST field. Figure as in Fig. 3a.

https://doi.org/10.5194/egusphere-2026-2794
Preprint. Discussion started: 11 June 2026
© Author(s) 2026. CC BY 4.0 License.

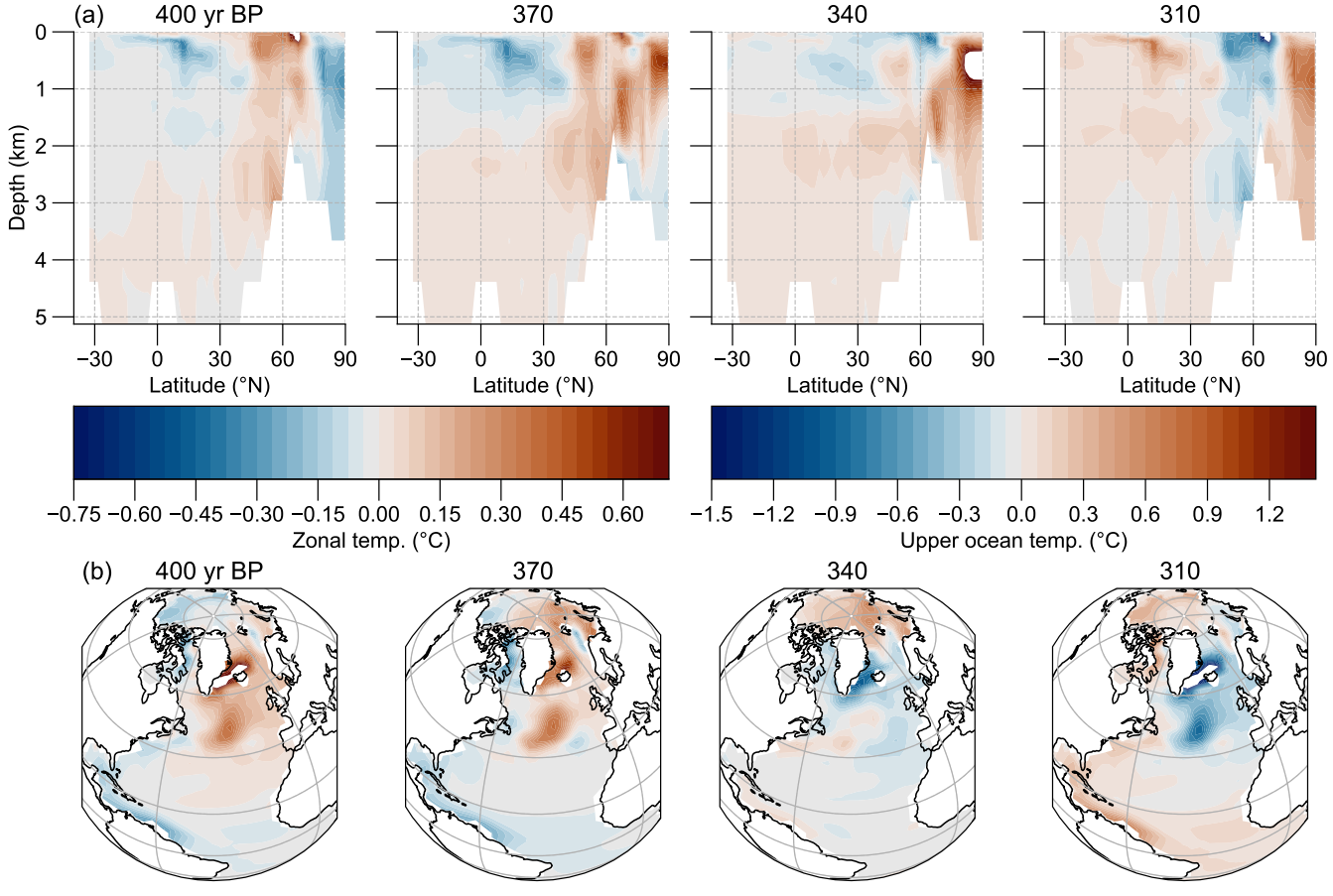


**Figure A4.** Spatio-temporal evolution of temperature anomalies associated with the 200-year mode over 30-year intervals. a) The zonally averaged mode is based on ST-RC 5-7 from the MSSA spectrum based on the joint zonally averaged salinity and temperature field and $M$ = 500 yr (Fig. 5a). b) The upper 300 m mode is based on ST-RC 5-6 from the MSSA spectrum based on the upper 300 m ocean temperature field and $M$ = 500 yr (Fig. 6a).

https://doi.org/10.5194/egusphere-2026-2794
Preprint. Discussion started: 11 June 2026
© Author(s) 2026. CC BY 4.0 License.

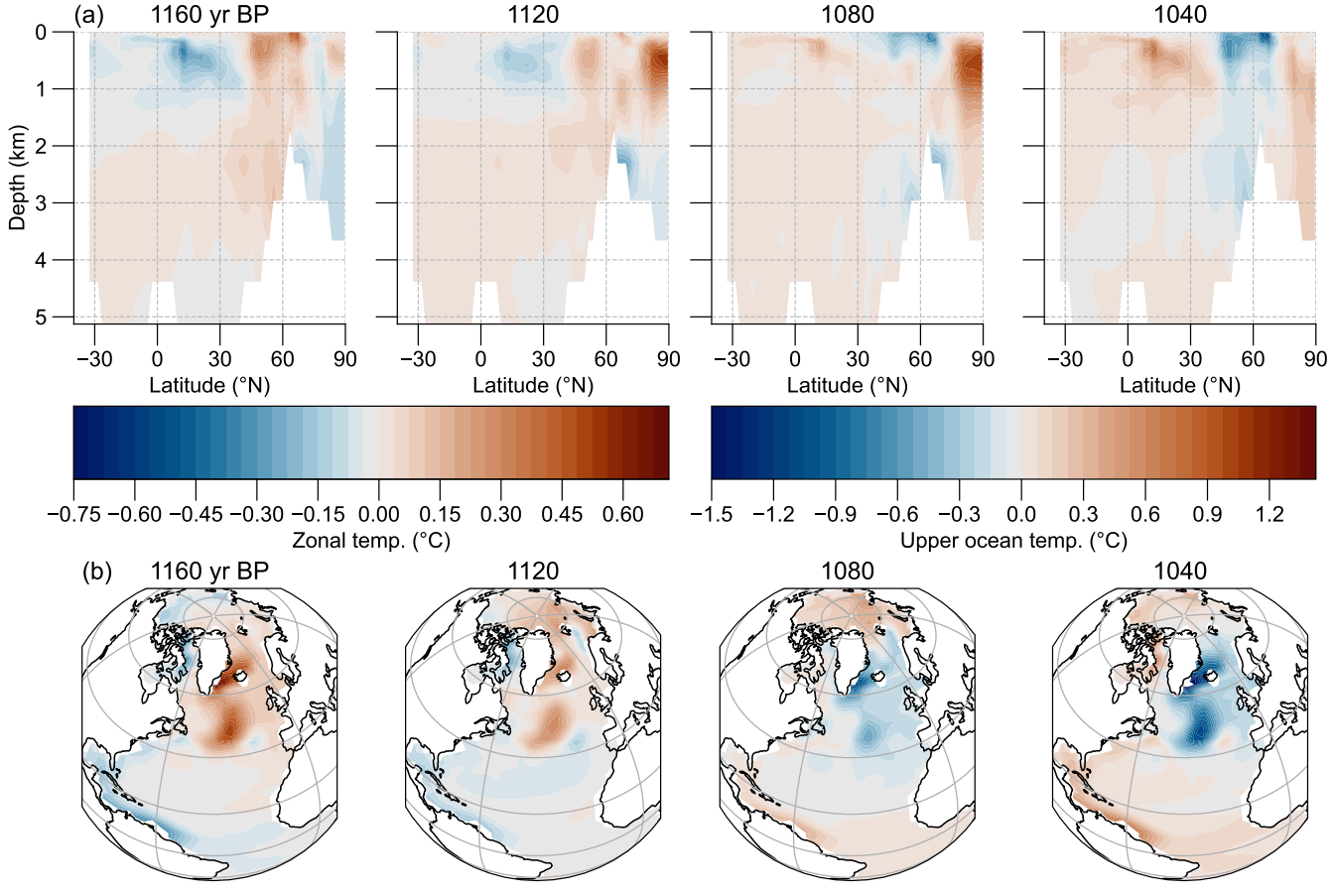


**Figure A5.** Spatio-temporal evolution of temperature anomalies associated with the 280-year mode over 40-year intervals. a) The zonally averaged mode is based on ST-RC 3-6 from the MSSA spectrum based on the joint zonally averaged salinity and temperature field and $M$ = 500 yr (Fig. 5a). b) The upper 300 m mode is based on ST-RC 3-4 from the MSSA spectrum based on the upper 300 m ocean temperature field and $M$ = 500 yr (Fig. 6a).

https://doi.org/10.5194/egusphere-2026-2794
Preprint. Discussion started: 11 June 2026
© Author(s) 2026. CC BY 4.0 License.

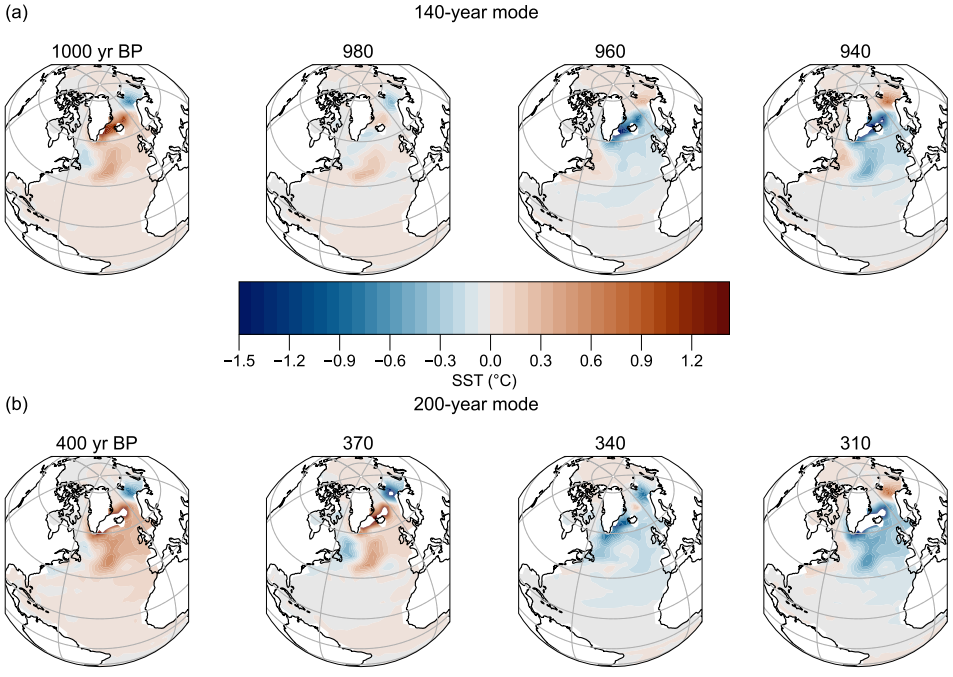


**Figure A6.** Spatio-temporal evolution of SST anomalies associated with the a) 140-year mode, and b) the 200-year mode from the MSSA spectrum based on the SST field and $M$ = 500 yr. The 140-year mode in panel a) is based on ST-RC 7-8, and the 200-year mode in panel b) on ST-RC 4-6 (Fig. A3c).

https://doi.org/10.5194/egusphere-2026-2794
Preprint. Discussion started: 11 June 2026
© Author(s) 2026. CC BY 4.0 License.

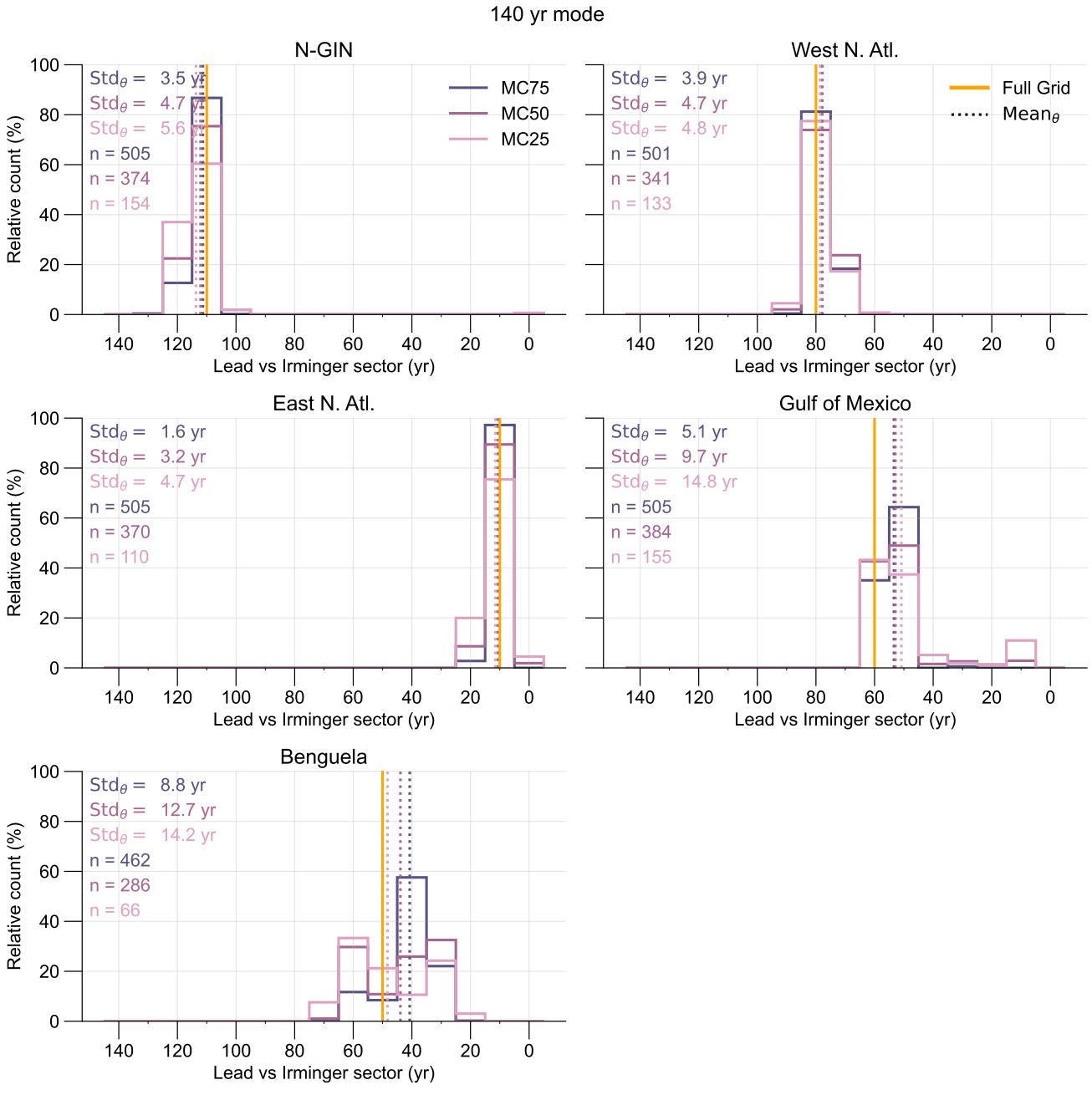


**Figure A7.** Spatio-temporal coherence of the 140-year mode between the Full Grid (orange) and the MC experiments (shades of pink) for a window size $M$ = 500 yr. Panels show the phase lead of the time-series computed over: the N-GIN, West N. Atlantic, East N. Atlantic, Gulf of Mexico, and Benguela sector. Figure as in Fig. 8.

https://doi.org/10.5194/egusphere-2026-2794
Preprint. Discussion started: 11 June 2026
© Author(s) 2026. CC BY 4.0 License.

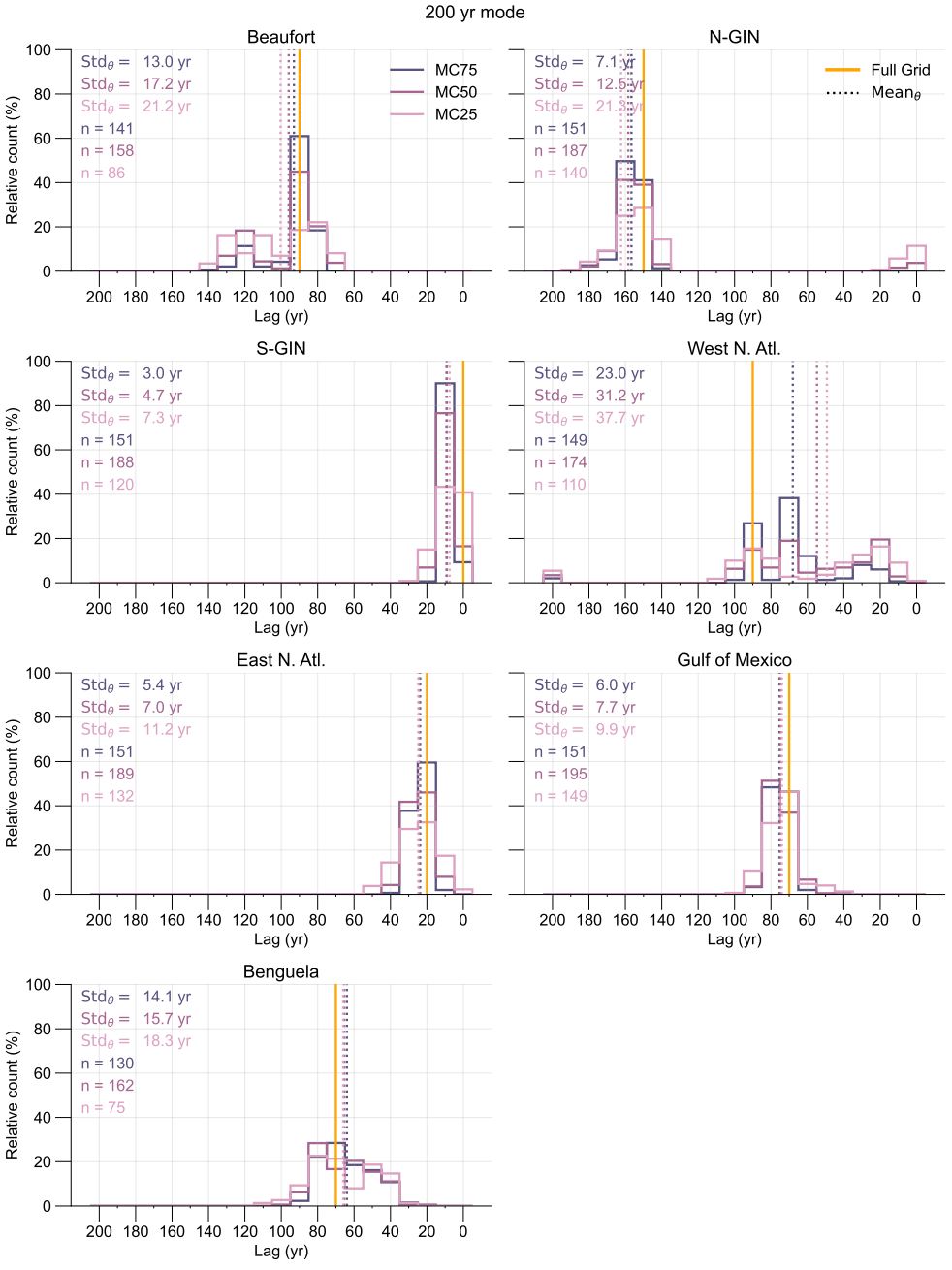


**Figure A8.** Spatio-temporal coherence of the 200-year mode between the Full Grid (orange) and the MC experiments (shades of pink) for a window size $M$ = 500 yr. Panels show the phase lead of the time-series computed over the different sectors as defined in Fig. 1). Figure as in Fig. 8.

https://doi.org/10.5194/egusphere-2026-2794
Preprint. Discussion started: 11 June 2026
© Author(s) 2026. CC BY 4.0 License.

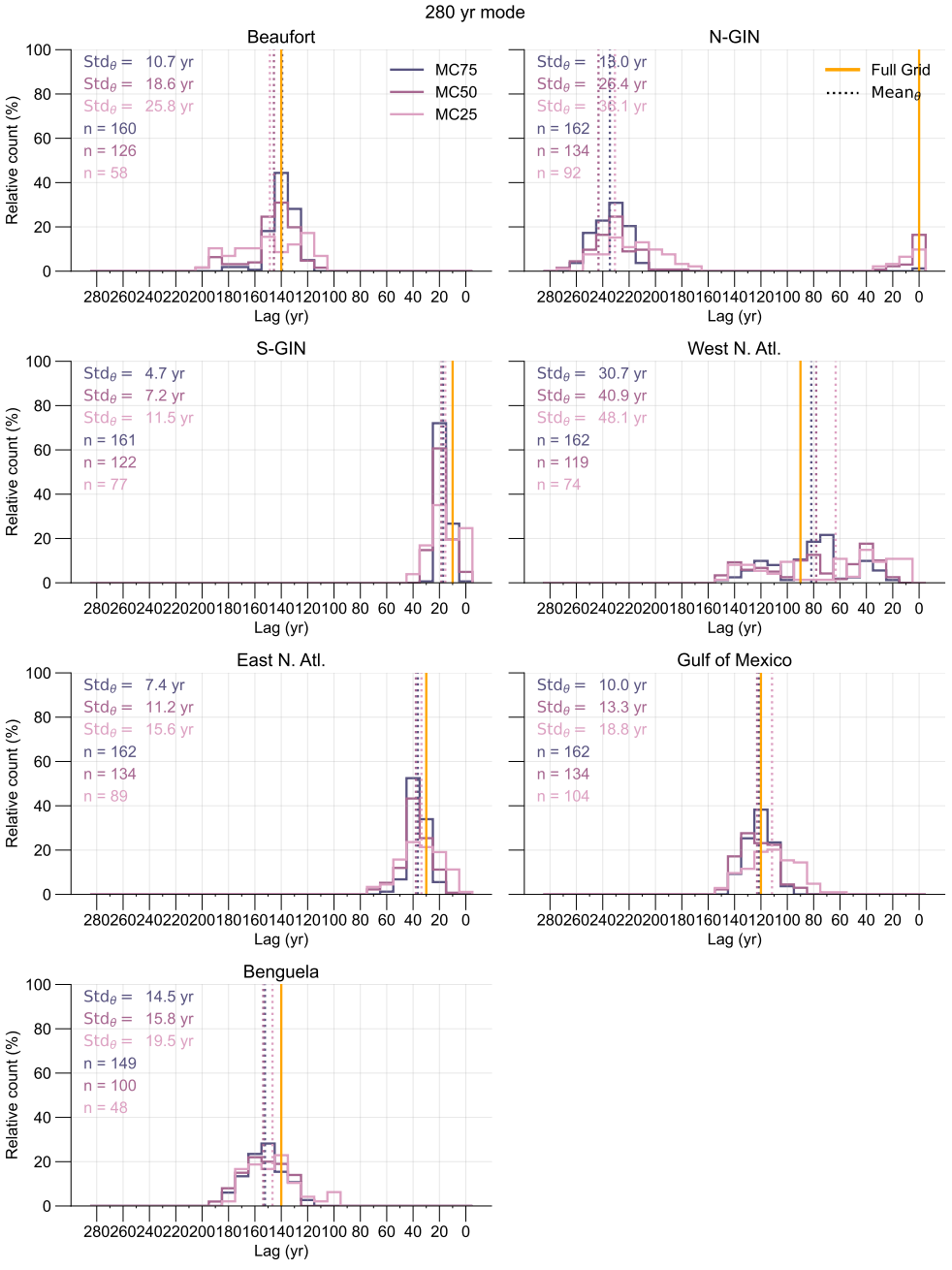


**Figure A9.** Spatio-temporal coherence of the 280-year mode between the Full Grid (orange) and the MC experiments (shades of pink) for a window size $M$ = 500 yr. Panels show the phase lead of the time-series computed over the different sectors as defined in Fig. 1). Figure as in Fig. 8.

https://doi.org/10.5194/egusphere-2026-2794
Preprint. Discussion started: 11 June 2026
© Author(s) 2026. CC BY 4.0 License.

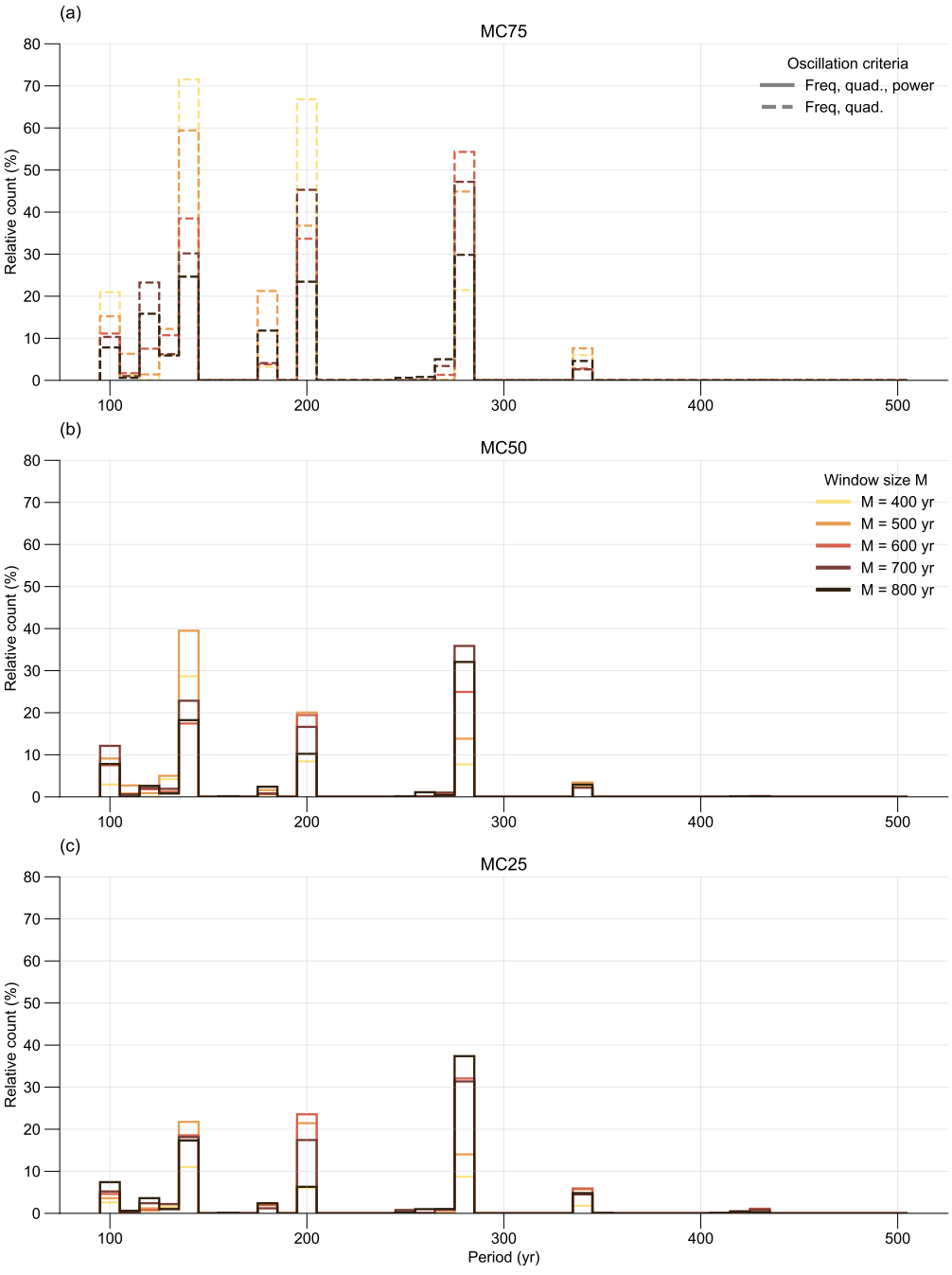


**Figure A10.** Relative frequency histograms that summarise the results for the MC experiments. Colours indicate different window sizes. The histograms indicate the percentage of MC realisations where an oscillatory mode is identified at a given period (x-axis). a) Sensitivity experiment where T-EOF pairs from MC75 are considered as oscillatory modes when the frequency and quadrature criteria are satisfied. Panels b) and c) summarise the results for MC50 (b) and MC25 (c) where T-EOF pairs must also satisfy the power criterium in addition to the frequency and quadrature criteria, similar to Fig. 7b.

**Table A1.** PAGES 2k temperature database records used to determine Proxy Grid locations. (Table is work in progress)

| dataSetName | DOI | paleoData_proxy | Lat | Lon | Elev (m) |
|---|---|---|---|---|---|
| Arc-MD992275.Jiang.2005 | 10.1130/G21130.1 | diatom | 66.550 | -17.700 | -470.0 |
| Arc-VoeringPlateau.Berner.2011 | 10.1029/2010PA002002 | diatom | 66.970 | 7.640 | -1048.0 |
| Ocn-AlboranSea384B.Nieto-Moreno.2013 | 10.1016/j.orggeochem.2012.11.001 | alkenone | 35.986 | -4.750 | -1022.0 |
| Ocn-AlboranSea436B.Nieto-Moreno.2013 | 10.1016/j.orggeochem.2012.11.001 | alkenone | 36.205 | -4.313 | -1108.0 |
| Ocn-CapeGhir.Doose-Rolinski.2007 | 10.1130/G23251A.1 | alkenone | 30.850 | -10.269 | -900.0 |
| Ocn-CapeGhir.McGregor.2007 | 10.1038/ngeo2510 | alkenone | 30.845 | -10.098 | -355.0 |
| Ocn-CapeHatteras.Cleroux.2008 | 10.1029/2007PA001505 | Mg/Ca | 34.973 | -75.201 | -620.0 |
| Ocn-CariacoBasin.Black.2007 | 10.1029/2007pa001427 | Mg/Ca | 10.770 | -64.770 | -450.0 |
| Ocn-DryTortugas.Lund.2006 | 10.1029/2005PA001218 | Mg/Ca | 24.590 | -83.580 | -530.0 |
| Ocn-DryTortugasA.Lund.2006 | 10.1029/2005PA001218 | Mg/Ca | 24.330 | -83.260 | -547.0 |
| Ocn-EasternTropicalNorthAtlantic.Kuhnert.2011 | 10.1029/2011pa002130 | Mg/Ca | 16.840 | -16.733 | -330.0 |
| Ocn-EmeraldBasin.Keigwin.2003 | 10.1007/s00382-003-0316-6 | alkenone | 45.890 | -62.800 | -250.0 |
| Ocn-EmeraldBasin.Keigwin.2007 | 10.1029/2006GL028495 | alkenone | 43.530 | -62.480 | -250.0 |
| Ocn-FeniDrift.Richter.2009 | 10.1016/j.quascirev.2009.04.008 | Mg/Ca | 55.500 | -13.900 | -2543.0 |
| Ocn-FiskBasin.Richey.2009 | 10.1029/2009GL040445 | Mg/Ca | 27.550 | -93.930 | -817.0 |
| Ocn-GarrisonBasin.Richey.2009 | 10.1029/2009GL040445 | Mg/Ca | 26.680 | -93.930 | -1570.0 |
| Ocn-GreatBahamaBank.Lund.2006 | 10.1029/2005PA001218 | Mg/Ca | 24.765 | -79.290 | -694.0 |
| Ocn-GreatBahamaBank.Richter.2006 | 10.1029/2005PA001218 | Mg/Ca | 24.580 | -79.260 | -531.0 |
| Ocn-GulfofGuinea.Weldeab.2007 | 10.1126/science.1140461 | Mg/Ca | 2.500 | 9.380 | -1295.0 |
| Ocn-MD95-2011.Grimalt.2002 | 10.1016/S0277-3791(01)00096-8 | alkenone | 66.970 | 7.630 | -1048.0 |
| Ocn-NorthIceland.Sicre.2011 | 10.1029/2011PA002169 | alkenone | 66.550 | -17.420 | -470.0 |
| Ocn-ODP984.Came.2007 | 10.1130/G23455A.1 | Mg/Ca | 61.430 | -24.085 | -1648.0 |
| Ocn-PigmyBasin.Richey.2015 | 10.1038/ngeo2510 | Mg/Ca | 27.200 | -91.420 | -2259.0 |
| Ocn-RAPiD-12-1K.Thornalley.2009 | 10.1038/nature07717 | Mg/Ca | 62.080 | -17.820 | -1938.0 |
| Ocn-SouthAtlanticWestAfrica.Leduc.2010 | 10.1029/2010GL044353 | alkenone | -29.140 | 16.720 | -97.0 |
| Ocn-SouthIceland.Sicre.2011 | 10.1029/2011PA002169 | alkenone | 57.450 | -27.910 | -2630.0 |
| Ocn-SubTropicalEasternNorthAtlantic.deMenocal.2000 | 10.1126/science.288.5474.2198 | foraminifera | 20.750 | -18.583 | -2263.0 |
| Ocn-TagusMudPatch.Abrantes.2005 | 10.1016/j.quascirev.2004.04.009 | alkenone | 38.556 | -9.350 | -96.0 |
| Ocn-WestSpitzberg.Bonnet.2010 | 10.1016/j.marmicro.2009.12.001 | dinocyst | 78.960 | 5.885 | -1497.0 |
| Ocn-WesternSvalbard.Spielhagen.2011 | 10.1126/science.1197397 | foraminifera | 78.910 | 6.770 | -1491.0 |



https://doi.org/10.5194/egusphere-2026-2794
Preprint. Discussion started: 11 June 2026
© Author(s) 2026. CC BY 4.0 License.

https://doi.org/10.5194/egusphere-2026-2794
Preprint. Discussion started: 11 June 2026
© Author(s) 2026. CC BY 4.0 License.

**Table A2.** Temperature 12k database records used to determine Proxy Grid locations. Part 1/2.

| dataSetName | DOI | paleoData_proxy | Lat | Lon | Elev (m) |
|---|---|---|---|---|---|
| B997_327.Castaneda.2004 | 10.1002/jqs.841 | d18O | 66.641 | -20.863 | -373.0 |
| D13882.Tierney | 10.1016/j.quascirev.2010.04.004 | alkenone | 38.635 | -9.454 | -88.0 |
| GGC19.Farmer.2011 | 10.1029/2011GL049714; 10.5194/cp-10-1605-2014 | — | 72.160 | -155.510 | -369.0 |
| GIK23258.Sarnthein.2003 | 10.1111/j.1502-3885.2003.tb01227.x; 10.5194/cp-10-1605-2014 | foraminifera | 75.000 | 14.000 | -1768.0 |
| GIK23258_2.Martrat.2003 | 10.1016/S0146-6380(03)00084-6 | d18O, alkenone | 74.998 | 13.969 | -1768.0 |
| GeoB1023_5.Kim.2002 | 10.1144/GSL.SP.1992.064.01.19; 10.1016/S0012-821X(01)00545-3 | d18O, alkenone | -17.157 | 11.012 | -1978.0 |
| GeoB5901_2.Kim.2004 | 10.1016/j.quascirev.2004.08.010 | alkenone | 36.380 | -7.071 | -574.0 |
| IOW225514BAY.Emeis.2003 | 10.1191/0959683603hl634rp | alkenone | 57.838 | 8.704 | -420.0 |
| JR51GC_35.Bendle.2007 | 10.1177/0959683607073269 | alkenone | 66.600 | -17.577 | -420.0 |
| KNR166_JPC26.Schmidt.2011 | 10.1016/j.epsl.2015.06.062; 10.1029/2011PA002157 | Mg/Ca, d18O | 24.327 | -83.252 | -546.0 |
| KNR166_JPC51.Schmidt.2012 | 10.1029/2012PA002284 | Mg/Ca, d18O | 24.412 | -83.219 | -198.0 |
| LO09-14.Berner.2008 | 10.5194/cp-10-1605-2014; 10.1029/2006PA001339 | diatom | 58.938 | -20.408 | -1685.0 |
| Lingreville.Billard.1995 | 10.3406/rao.1995.1026; 10.1038/nature25464 | pollen | 48.930 | -1.540 | +5.0 |
| MD95_2011.Risebrobakken.2003 | 10.1029/2002PA000764 | d18O | 66.970 | 7.639 | -1048.0 |
| MD95_2011Assemblage.Risebrobakken.2003 | 10.1016/S0277-3791(01)00096-8; 10.1029/2002PA000764; 10.5194/cp-6-179-2010; 10.2312/reports-ifg.1999.3 | foraminifera, radiolaria, alkenone | 66.970 | 7.639 | -1048.0 |

https://doi.org/10.5194/egusphere-2026-2794
Preprint. Discussion started: 11 June 2026
© Author(s) 2026. CC BY 4.0 License.

**Table A3.** Temperature 12k database records used to determine Proxy Grid locations. Part 2/2.

| dataSetName | DOI | paleoData_proxy | Lat | Lon | Elev (m) |
|---|---|---|---|---|---|
| MD95_2015.Marchal.2002 | 10.1016/S0277-3791(01)00105-6 10.1029/2011PA002117; | alkenone | 58.762 | -25.959 | -2630.0 |
| MD99-2284.Risebrobakken.2009 | 10.1016/j.quascirev.2014.06.028 10.5194/cp-10-1605-2014; | foraminifera | 62.367 | 0.967 | -1500.0 |
| MD99-2322.Jennings.2011 | 10.1016/j.quascirev.2011.01.016 10.1029/2008GC002199; | foraminifera | 67.136 | -30.828 | -714.0 |
| MD99_2251.Farmer.2008 | 10.1126/science.1127213 10.1177/0959683616652703; | d18O, Mg/Ca | 57.448 | -27.908 | -2620.0 |
| MD99_2269.Kristjnsd_ttir.2017 | 10.1029/2006PA001285 | Mg/Ca, alkenone, d18O | 66.641 | -20.863 | -365.0 |
| MD99_2339.Eynaud.2009 | 10.1029/2009GC002398 10.1016/j.margeo.2014.05.009; | d18O | 35.886 | -7.528 | -1177.0 |
| MSM05_5_712_2.Werner.2013 | 10.1002/palo.20028 10.1029/2004PA001074; | d18O, Mg/Ca | 78.916 | 6.767 | -1389.0 |
| OCE326_GGC26.Keigwin.2005 | 10.1029/2006GL028495 | d18O, alkenone | 43.483 | -54.866 | -3975.0 |
| OCE326_GGC30.Sachs.2007 | 10.1029/2006GL028495 10.1038/ngeo227; | alkenone | 43.885 | -62.795 | -240.0 |
| ODP162_984.Came.2007 | 10.1130/G23455A.1 | d18O, Mg/Ca | 61.425 | -24.082 | -1648.0 |
| ODP_175_1084B.Farmer.2005 | 10.1029/2004PA001049 10.1016/j.quascirev.2011.07.025; | Mg/Ca | -25.514 | 13.028 | -1992.0 |
| P1003.Sejrup.2011 | 10.5194/cp-10-1605-2014 | d18O | 63.762 | 5.255 | -875.0 |
| PP10-07.Mary.2016 | 10.5194/cp-2016-32; — | foraminifera | 43.677 | -2.228 | -1472.0 |
| PSh-5159N.Risebrobakken.2011 | 10.1029/2011PA002117 10.1038/nature07717; | alkenone | 71.350 | 22.633 | -422.0 |
| RAPiD_12_1K.Thornalley.2010 | 10.1029/2009PA001833 10.1016/j.margeo.2011.11.004; | d18O, Mg/Ca | 62.091 | -17.820 | -1938.0 |
| Station803.Bringue.2012 | 10.1016/j.quascirev.2013.07.006 | —, dinocyst | 70.633 | -135.880 | -218.0 |

https://doi.org/10.5194/egusphere-2026-2794
Preprint. Discussion started: 11 June 2026
© Author(s) 2026. CC BY 4.0 License.

*Author contributions.* TB - conceptualization, data curation, formal analysis, visualisation, writing (original draft preparation), writing (review and editing). HAD, conceptualization, funding acquisition, writing (review and editing). PB, conceptualization, investigation (*i*LOVECLIM simulation), funding acquisition, writing (review and editing).

*Competing interests.* The authors declare that they have no conflict of interest.

*Acknowledgements.* We thank N. J. de Winter and M. Cini for their valuable feedback.

https://doi.org/10.5194/egusphere-2026-2794
Preprint. Discussion started: 11 June 2026
© Author(s) 2026. CC BY 4.0 License.

## References

Allen, M. R. and Robertson, A. W.: Distinguishing Modulated Oscillations from Coloured Noise in Multivariate Datasets, Climate Dynamics, 12, 775–784, https://doi.org/10.1007/s003820050142, 1996.

Allen, M. R. and Smith, L. A.: Monte Carlo SSA: Detecting Irregular Oscillations in the Presence of Colored Noise, Journal of Climate, 9, 3373–3404, 1996.

Anchukaitis, K. J. and Tierney, J. E.: Identifying Coherent Spatiotemporal Modes in Time-Uncertain Proxy Paleoclimate Records, Climate Dynamics, 41, 1291–1306, https://doi.org/10.1007/s00382-012-1483-0, 2013.

Anchukaitis, K. J., Wilson, R., Briffa, K. R., Büntgen, U., Cook, E. R., D'Arrigo, R., Davi, N., Esper, J., Frank, D., Gunnarson, B. E., Hegerl, G., Helama, S., Klesse, S., Krusic, P. J., Linderholm, H. W., Myglan, V., Osborn, T. J., Zhang, P., Rydval, M., Schneider, L., Schurer, A., Wiles, G., and Zorita, E.: Last Millennium Northern Hemisphere Summer Temperatures from Tree Rings: Part II, Spatially Resolved Reconstructions, Quaternary Science Reviews, 163, 1–22, https://doi.org/10.1016/j.quascirev.2017.02.020, 2017.

Andree, M.: The Impact of Bioturbation on Ams$^{14}$ C Dates On Handpicked Foraminifera: A Statistical Model, Radiocarbon, 29, 169–175, https://doi.org/10.1017/S0033822200056927, 1987.

Ashok, K., Behera, S. K., Rao, S. A., Weng, H., and Yamagata, T.: El Niño Modoki and Its Possible Teleconnection, Journal of Geophysical Research: Oceans, 112, 2006JC003 798, https://doi.org/10.1029/2006JC003798, 2007.

Askjær, T. G., Zhang, Q., Schenk, F., Ljungqvist, F. C., Lu, Z., Brierley, C. M., Hopcroft, P. O., Jungclaus, J., Shi, X., Lohmann, G., Sun, W., Liu, J., Braconnot, P., Otto-Bliesner, B. L., Wu, Z., Yin, Q., Kang, Y., and Yang, H.: Multi-Centennial Holocene Climate Variability in Proxy Records and Transient Model Simulations, Quaternary Science Reviews, 296, 107 801, https://doi.org/10.1016/j.quascirev.2022.107801, 2022.

Ayache, M., Swingedouw, D., Mary, Y., Eynaud, F., and Colin, C.: Multi-Centennial Variability of the AMOC over the Holocene: A New Reconstruction Based on Multiple Proxy-Derived SST Records, Global and Planetary Change, 170, 172–189, https://doi.org/10.1016/j.gloplacha.2018.08.016, 2018.

Bakker, P., Goosse, H., and Roche, D. M.: Internal Climate Variability and Spatial Temperature Correlations during the Past 2000 Years, Climate of the Past, 18, 2523–2544, https://doi.org/10.5194/cp-18-2523-2022, 2022.

Bakker, P., Bense, T. T., Lubbe, H. J. V. D., and Roche, D. M.: On the Detectability of Multi-Centennial AMOC Variations, https://doi.org/10.22541/essoar.177172623.34981497/v1, 2026.

Bense, T.: Data for Publication: Extracting Coherent Spatio-Temporal Modes of Simulated Multi-Centennial AMOC Variability under Constraints That Reflect Sparsity of Proxy Data, https://doi.org/10.5281/ZENODO.20122668, 2026a.

Bense, T. T.: Tbense/Bense_ea_2026_Extracting_coherent_spatio: Notebooks for Submission Bense et al. (2026) Clim. of the Past, Zenodo, https://doi.org/10.5281/ZENODO.20201057, 2026b.

Berger, AndréL.: Long-Term Variations of Daily Insolation and Quaternary Climatic Changes, Journal of the Atmospheric Sciences, 35, 2362–2367, https://doi.org/10.1175/1520-0469(1978)035<2362:LTVODI>2.0.CO;2, 1978.

Berger, W. H. and Heath, G. R.: Vertical Mixing in Pelagic Sediments, Journal of Marine Research, 26, 1968.

Bouttes, N., Roche, D. M., Mariotti, V., and Bopp, L.: Including an Ocean Carbon Cycle Model into *i* LOVECLIM (v1.0), Geoscientific Model Development, 8, 1563–1576, https://doi.org/10.5194/gmd-8-1563-2015, 2015.

Broomhead, D. S. and King, G. P.: Extracting Qualitative Dynamics from Experimental Data, Physica D: Nonlinear Phenomena, 20, 217–236, https://doi.org/10.1016/0167-2789(86)90031-X, 1986a.

https://doi.org/10.5194/egusphere-2026-2794
Preprint. Discussion started: 11 June 2026
© Author(s) 2026. CC BY 4.0 License.

Broomhead, D. S. and King, G. P.: On the Qualitative Analysis of Experimental Dynamical Systems, in: Nonlinear Phenomena and Chaos, edited by Sarkar, S., pp. 113–144, Adam Hilger Ltd, Bristol, England, 1986b.

Brovkin, V., Ganopolski, A., and Svirezhev, Y.: A Continuous Climate-Vegetation Classification for Use in Climate-Biosphere Studies, Ecological Modelling, 101, 251–261, https://doi.org/10.1016/S0304-3800(97)00049-5, 1997.

Campin, J.-M. and Goosse, H.: Parameterization of Density-Driven Downsloping Flow for a Coarse-Resolution Ocean Model in z-Coordinate, Tellus A, 51, 412–430, https://doi.org/10.1034/j.1600-0870.1999.t01-3-00006.x, 1999.

Cao, N., Zhang, Q., Power, K. E., Schenk, F., Wyser, K., and Yang, H.: The Role of Internal Feedbacks in Sustaining Multi-Centennial Variability of the Atlantic Meridional Overturning Circulation Revealed by EC-Earth3-LR Simulations, Earth and Planetary Science Letters, 621, 118 372, https://doi.org/10.1016/j.epsl.2023.118372, 2023.

Christiansen, B. and Ljungqvist, F. C.: Challenges and Perspectives for Large-scale Temperature Reconstructions of the Past Two Millennia, Reviews of Geophysics, 55, 40–96, https://doi.org/10.1002/2016RG000521, 2017.

Crameri, F., Shephard, G. E., and Heron, P. J.: The Misuse of Colour in Science Communication, Nature Communications, 11, 5444, https://doi.org/10.1038/s41467-020-19160-7, 2020.

Dansgaard, W., Johnsen, S. J., Clausen, H. B., Dahl-Jensen, D., Gundestrup, N. S., Hammer, C. U., Hvidberg, C. S., Steffensen, J. P., Sveinbjörnsdottir, A. E., Jouzel, J., and Bond, G.: Evidence for General Instability of Past Climate from a 250-Kyr Ice-Core Record, Nature, 364, 218–220, https://doi.org/10.1038/364218a0, 1993.

Delworth, T. L. and Zeng, F.: Multicentennial Variability of the Atlantic Meridional Overturning Circulation and Its Climatic Influence in a 4000 Year Simulation of the GFDL CM2.1 Climate Model, Geophysical Research Letters, 39, 2012GL052 107, https://doi.org/10.1029/2012GL052107, 2012.

Deser, C., Knutti, R., Solomon, S., and Phillips, A. S.: Communication of the Role of Natural Variability in Future North American Climate, Nature Climate Change, 2, 775–779, https://doi.org/10.1038/nclimate1562, 2012a.

Deser, C., Phillips, A., Bourdette, V., and Teng, H.: Uncertainty in Climate Change Projections: The Role of Internal Variability, Climate Dynamics, 38, 527–546, https://doi.org/10.1007/s00382-010-0977-x, 2012b.

Dijkstra, H. A., Te Raa, L., Schmeits, M., and Gerrits, J.: On the Physics of the Atlantic Multidecadal Oscillation, Ocean Dynamics, 56, 36–50, https://doi.org/10.1007/s10236-005-0043-0, 2006.

Ellerhoff, B. and Rehfeld, K.: Probing the Timescale Dependency of Local and Global Variations in Surface Air Temperature from Climate Simulations and Reconstructions of the Last Millennia, Physical Review E, 104, 064 136, https://doi.org/10.1103/PhysRevE.104.064136, 2021.

Franke, J. G. and Donner, R. V.: Correlating Paleoclimate Time Series: Sources of Uncertainty and Potential Pitfalls, Quaternary Science Reviews, 212, 69–79, https://doi.org/10.1016/j.quascirev.2019.03.017, 2019.

Frankignoul, C. and Hasselmann, K.: Stochastic Climate Models, Part II Application to Sea-Surface Temperature Anomalies and Thermocline Variability, Tellus, 29, 289–305, https://doi.org/10.1111/j.2153-3490.1977.tb00740.x, 1977.

Friedrich, T., Timmermann, A., Menviel, L., Elison Timm, O., Mouchet, A., and Roche, D. M.: The Mechanism behind Internally Generated Centennial-to-Millennial Scale Climate Variability in an Earth System Model of Intermediate Complexity, Geoscientific Model Development, 3, 377–389, https://doi.org/10.5194/gmd-3-377-2010, 2010.

Gent, P. R. and McWilliams, J. C.: Isopycnal Mixing in Ocean Circulation Models, Journal of Physical Oceanography, 20, 150–155, https://doi.org/10.1175/1520-0485(1990)020<0150:IMIOCM>2.0.CO;2, 1990.

https://doi.org/10.5194/egusphere-2026-2794
Preprint. Discussion started: 11 June 2026
© Author(s) 2026. CC BY 4.0 License.

Ghil, M., Allen, M. R., Dettinger, M. D., Ide, K., Kondrashov, D., Mann, M. E., Robertson, A. W., Saunders, A., Tian, Y., Varadi, F., and Yiou, P.: ADVANCED SPECTRAL METHODS FOR CLIMATIC TIME SERIES, Reviews of Geophysics, 40, https://doi.org/10.1029/2000RG000092, 2002.

Goosse, H., Brovkin, V., Fichefet, T., Haarsma, R., Huybrechts, P., Jongma, J., Mouchet, A., Selten, F., Barriat, P.-Y., Campin, J.-M., Deleersnijder, E., Driesschaert, E., Goelzer, H., Janssens, I., Loutre, M.-F., Morales Maqueda, M. A., Opsteegh, T., Mathieu, P.-P., Munhoven, G., Pettersson, E. J., Renssen, H., Roche, D. M., Schaeffer, M., Tartinville, B., Timmermann, A., and Weber, S. L.: Description of the Earth System Model of Intermediate Complexity LOVECLIM Version 1.2, Geoscientific Model Development, 3, 603–633, https://doi.org/10.5194/gmd-3-603-2010, 2010.

Groth, A. and Ghil, M.: Multivariate Singular Spectrum Analysis and the Road to Phase Synchronization, Physical Review E, 84, 036 206, https://doi.org/10.1103/PhysRevE.84.036206, 2011.

Groth, A. and Ghil, M.: Monte Carlo Singular Spectrum Analysis (SSA) Revisited: Detecting Oscillator Clusters in Multivariate Datasets, Journal of Climate, 28, 7873–7893, https://doi.org/10.1175/JCLI-D-15-0100.1, 2015.

Groth, A., Feliks, Y., Kondrashov, D., and Ghil, M.: Interannual Variability in the North Atlantic Ocean's Temperature Field and Its Association with the Wind Stress Forcing, Journal of Climate, 30, 2655–2678, https://doi.org/10.1175/JCLI-D-16-0370.1, 2017.

Hadley Centre for Climate Prediction and Research//Ministry of Defence/United Kingdom and Office, M.: Hadley Centre Global Sea Ice and Sea Surface Temperature (HadISST), https://doi.org/10.5065/XMYE-AN84, 2000.

Hasselmann, K.: Stochastic Climate Models: Part I. Theory, Tellus A: Dynamic Meteorology and Oceanography, 28, 473, https://doi.org/10.3402/tellusa.v28i6.11316, 1976.

Hébert, R., Herzschuh, U., and Laepple, T.: Millennial-Scale Climate Variability over Land Overprinted by Ocean Temperature Fluctuations, Nature Geoscience, 15, 899–905, https://doi.org/10.1038/s41561-022-01056-4, 2022.

Hutson, W. H.: Bioturbation of Deep-Sea Sediments: Oxygen Isotopes and Stratigraphic Uncertainty, Geology, 8, 127, https://doi.org/10.1130/0091-7613(1980)8<127:BODSOI>2.0.CO;2, 1980.

Jaume-Santero, F., Barriopedro, D., García-Herrera, R., Calvo, N., and Salcedo-Sanz, S.: Selection of Optimal Proxy Locations for Temperature Field Reconstructions Using Evolutionary Algorithms, Scientific Reports, 10, 7900, https://doi.org/10.1038/s41598-020-64459-6, 2020.

Jiang, N., Neelin, J. D., and Ghil, M.: Quasi-Quadrennial and Quasi-Biennial Variability in the Equatorial Pacific, Climate Dynamics, 12, 101–112, https://doi.org/10.1007/BF00223723, 1995.

Jiang, W., Gastineau, G., and Codron, F.: Multicentennial Variability Driven by Salinity Exchanges Between the Atlantic and the Arctic Ocean in a Coupled Climate Model, Journal of Advances in Modeling Earth Systems, 13, e2020MS002 366, https://doi.org/10.1029/2020MS002366, 2021.

Kanzow, T., Cunningham, S. A., Johns, W. E., Hirschi, J. J.-M., Marotzke, J., Baringer, M. O., Meinen, C. S., Chidichimo, M. P., Atkinson, C., Beal, L. M., Bryden, H. L., and Collins, J.: Seasonal Variability of the Atlantic Meridional Overturning Circulation at 26.5°N, Journal of Climate, 23, 5678–5698, https://doi.org/10.1175/2010JCLI3389.1, 2010.

Kaufman, D., McKay, N., Routson, C., Erb, M., Davis, B., Heiri, O., Jaccard, S., Tierney, J., Dätwyler, C., Axford, Y., Brussel, T., Cartapanis, O., Chase, B., Dawson, A., De Vernal, A., Engels, S., Jonkers, L., Marsicek, J., Moffa-Sánchez, P., Morrill, C., Orsi, A., Rehfeld, K., Saunders, K., Sommer, P. S., Thomas, E., Tonello, M., Tóth, M., Vachula, R., Andreev, A., Bertrand, S., Biskaborn, B., Bringué, M., Brooks, S., Caniupán, M., Chevalier, M., Cwynar, L., Emile-Geay, J., Fegyveresi, J., Feurdean, A., Finsinger, W., Fortin, M.-C., Foster, L., Fox, M., Gajewski, K., Grosjean, M., Hausmann, S., Heinrichs, M., Holmes, N., Ilyashuk, B., Ilyashuk, E., Juggins, S., Khider, D.,

https://doi.org/10.5194/egusphere-2026-2794
Preprint. Discussion started: 11 June 2026
© Author(s) 2026. CC BY 4.0 License.

Koinig, K., Langdon, P., Larocque-Tobler, I., Li, J., Lotter, A., Luoto, T., Mackay, A., Magyari, E., Malevich, S., Mark, B., Massaferro, J., Montade, V., Nazarova, L., Novenko, E., Pařil, P., Pearson, E., Peros, M., Pienitz, R., Płóciennik, M., Porinchu, D., Potito, A., Rees, A., Reinemann, S., Roberts, S., Rolland, N., Salonen, S., Self, A., Seppä, H., Shala, S., St-Jacques, J.-M., Stenni, B., Syrykh, L., Tarrats, P., Taylor, K., Van Den Bos, V., Velle, G., Wahl, E., Walker, I., Wilmshurst, J., Zhang, E., and Zhilich, S.: A Global Database of Holocene Paleotemperature Records, Scientific Data, 7, 115, https://doi.org/10.1038/s41597-020-0445-3, 2020.

Keppenne, C. L. and Ghil, M.: Adaptive Filtering and Prediction of the Southern Oscillation Index, Journal of Geophysical Research: Atmospheres, 97, 20 449–20 454, https://doi.org/10.1029/92JD02219, 1992.

Kessler, A., Bouttes, N., Roche, D. M., Ninnemann, U. S., and Tjiputra, J.: Dynamics of Spontaneous (Multi) Centennial-Scale Variations of the Atlantic Meridional Overturning Circulation Strength During the Last Interglacial, Paleoceanography and Paleoclimatology, 35, e2020PA003 913, https://doi.org/10.1029/2020PA003913, 2020.

Krieger, S. and Freij, N.: PyCWT: Wavelet Spectral Analysis in Python., 2025.

Kushnir, Y.: Interdecadal Variations in North Atlantic Sea Surface Temperature and Associated Atmospheric Conditions, Journal of Climate, 7, 141–157, https://doi.org/10.1175/1520-0442(1994)007<0141:IVINAS>2.0.CO;2, 1994.

Laepple, T. and Huybers, P.: Ocean Surface Temperature Variability: Large Model–Data Differences at Decadal and Longer Periods, Proceedings of the National Academy of Sciences, 111, 16 682–16 687, https://doi.org/10.1073/pnas.1412077111, 2014.

Laepple, T., Ziegler, E., Weitzel, N., Hébert, R., Ellerhoff, B., Schoch, P., Martrat, B., Bothe, O., Moreno-Chamarro, E., Chevalier, M., Herbert, A., and Rehfeld, K.: Regional but Not Global Temperature Variability Underestimated by Climate Models at Supradecadal Timescales, Nature Geoscience, 16, 958–966, https://doi.org/10.1038/s41561-023-01299-9, 2023.

Latif, M., Martin, T., and Park, W.: Southern Ocean Sector Centennial Climate Variability and Recent Decadal Trends, Journal of Climate, 26, 7767–7782, https://doi.org/10.1175/JCLI-D-12-00281.1, 2013.

Lehner, F. and Deser, C.: Origin, Importance, and Predictive Limits of Internal Climate Variability, Environmental Research: Climate, 2, 023 001, https://doi.org/10.1088/2752-5295/accf30, 2023.

Li, Y. and Yang, H.: A Theory for Self-Sustained Multicentennial Oscillation of the Atlantic Meridional Overturning Circulation, Journal of Climate, 35, 5883–5896, https://doi.org/10.1175/JCLI-D-21-0685.1, 2022.

Liu, Y., San Liang, X., and Weisberg, R. H.: Rectification of the Bias in the Wavelet Power Spectrum, Journal of Atmospheric and Oceanic Technology, 24, 2093–2102, https://doi.org/10.1175/2007JTECHO511.1, 2007.

Lougheed, B. C., Ascough, P., Dolman, A. M., Löwemark, L., and Metcalfe, B.: Re-Evaluating$^{14}$ C Dating Accuracy in Deep-Sea Sediment Archives, Geochronology, 2, 17–31, https://doi.org/10.5194/gchron-2-17-2020, 2020.

Lovejoy, S., Schertzer, D., and Varon, D.: Do GCMs Predict the Climate ... or Macroweather?, Earth System Dynamics, 4, 439–454, https://doi.org/10.5194/esd-4-439-2013, 2013.

Löwemark, L.: Disturb, Distort, Destroy – How Burrowing Organisms Bias Paleoclimatic Time Series, Ichnos, 32, 73–83, https://doi.org/10.1080/10420940.2025.2495407, 2025.

Mann, M. E. and Lees, J. M.: Robust Estimation of Background Noise and Signal Detection in Climatic Time Series, Climatic Change, 33, 409–445, https://doi.org/10.1007/BF00142586, 1996.

Manta, G., Bach, E., Talento, S., Barreiro, M., Speich, S., and Ghil, M.: The South Atlantic Dipole via Multichannel Singular Spectrum Analysis, Scientific Reports, 14, 15 534, https://doi.org/10.1038/s41598-024-62089-w, 2024.

Mardia, K. V. and Jupp, P. E.: Directional Statistics, Wiley Series in Probability and Statistics, Wiley, 1 edn., https://doi.org/10.1002/9780470316979, 1999.

https://doi.org/10.5194/egusphere-2026-2794
Preprint. Discussion started: 11 June 2026
© Author(s) 2026. CC BY 4.0 License.

Marotzke, J.: From Theory to RAPID AMOC Observations: A Personal Voyage of Discovery, Philosophical Transactions of the Royal Society A: Mathematical, Physical and Engineering Sciences, 381, 20220 192, https://doi.org/10.1098/rsta.2022.0192, 2023.

Martin, T., Park, W., and Latif, M.: Southern Ocean Forcing of the North Atlantic at Multi-Centennial Time Scales in the Kiel Climate Model, Deep Sea Research Part II: Topical Studies in Oceanography, 114, 39–48, https://doi.org/10.1016/j.dsr2.2014.01.018, 2015.

Meccia, V. L., Fuentes-Franco, R., Davini, P., Bellomo, K., Fabiano, F., Yang, S., and Von Hardenberg, J.: Internal Multi-Centennial Variability of the Atlantic Meridional Overturning Circulation Simulated by EC-Earth3, Climate Dynamics, 60, 3695–3712, https://doi.org/10.1007/s00382-022-06534-4, 2023.

Mehling, O.: Analysis Code for "Centennial-scale Variability of the Atlantic Meridional Overturning Circulation in CMIP6 Models Shaped by Arctic–North Atlantic Interactions and Sea Ice Biases", Zenodo, https://doi.org/10.5281/ZENODO.11640570, 2024.

Mehling, O., Bellomo, K., Angeloni, M., Pasquero, C., and Von Hardenberg, J.: High-Latitude Precipitation as a Driver of Multicentennial Variability of the AMOC in a Climate Model of Intermediate Complexity, Climate Dynamics, 61, 1519–1534, https://doi.org/10.1007/s00382-022-06640-3, 2023.

Mehling, O., Bellomo, K., and Von Hardenberg, J.: Centennial-Scale Variability of the Atlantic Meridional Overturning Circulation in CMIP6 Models Shaped by Arctic–North Atlantic Interactions and Sea Ice Biases, Geophysical Research Letters, 51, e2024GL110 791, https://doi.org/10.1029/2024GL110791, 2024.

Missiaen, L., Bouttes, N., Roche, D. M., Dutay, J.-C., Quiquet, A., Waelbroeck, C., Pichat, S., and Peterschmitt, J.-Y.: Carbon Isotopes and Pa/Th Response to Forced Circulation Changes: A Model Perspective, Climate of the Past, 16, 867–883, https://doi.org/10.5194/cp-16-867-2020, 2020.

Moffa-Sánchez, P., Born, A., Hall, I. R., Thornalley, D. J. R., and Barker, S.: Solar Forcing of North Atlantic Surface Temperature and Salinity over the Past Millennium, Nature Geoscience, 7, 275–278, https://doi.org/10.1038/ngeo2094, 2014.

Moffa-Sánchez, P., Moreno-Chamarro, E., Reynolds, D. J., Ortega, P., Cunningham, L., Swingedouw, D., Amrhein, D. E., Halfar, J., Jonkers, L., Jungclaus, J. H., Perner, K., Wanamaker, A., and Yeager, S.: Variability in the Northern North Atlantic and Arctic Oceans Across the Last Two Millennia: A Review, Paleoceanography and Paleoclimatology, 34, 1399–1436, https://doi.org/10.1029/2018PA003508, 2019.

PAGES2k Consortium, Emile-Geay, J., McKay, N. P., Kaufman, D. S., Von Gunten, L., Wang, J., Anchukaitis, K. J., Abram, N. J., Addison, J. A., Curran, M. A., Evans, M. N., Henley, B. J., Hao, Z., Martrat, B., McGregor, H. V., Neukom, R., Pederson, G. T., Stenni, B., Thirumalai, K., Werner, J. P., Xu, C., Divine, D. V., Dixon, B. C., Gergis, J., Mundo, I. A., Nakatsuka, T., Phipps, S. J., Routson, C. C., Steig, E. J., Tierney, J. E., Tyler, J. J., Allen, K. J., Bertler, N. A., Björklund, J., Chase, B. M., Chen, M.-T., Cook, E., De Jong, R., DeLong, K. L., Dixon, D. A., Ekaykin, A. A., Ersek, V., Filipsson, H. L., Francus, P., Freund, M. B., Frezzotti, M., Gaire, N. P., Gajewski, K., Ge, Q., Goosse, H., Gornostaeva, A., Grosjean, M., Horiuchi, K., Hormes, A., Husum, K., Isaksson, E., Kandasamy, S., Kawamura, K., Kilbourne, K. H., Koç, N., Leduc, G., Linderholm, H. W., Lorrey, A. M., Mikhalenko, V., Mortyn, P. G., Motoyama, H., Moy, A. D., Mulvaney, R., Munz, P. M., Nash, D. J., Oerter, H., Opel, T., Orsi, A. J., Ovchinnikov, D. V., Porter, T. J., Roop, H. A., Saenger, C., Sano, M., Sauchyn, D., Saunders, K. M., Seidenkrantz, M.-S., Severi, M., Shao, X., Sicre, M.-A., Sigl, M., Sinclair, K., St. George, S., St. Jacques, J.-M., Thamban, M., Kuwar Thapa, U., Thomas, E. R., Turney, C., Uemura, R., Viau, A. E., Vladimirova, D. O., Wahl, E. R., White, J. W., Yu, Z., and Zinke, J.: A Global Multiproxy Database for Temperature Reconstructions of the Common Era, Scientific Data, 4, 170 088, https://doi.org/10.1038/sdata.2017.88, 2017.

Park, W. and Latif, M.: Multidecadal and Multicentennial Variability of the Meridional Overturning Circulation, Geophysical Research Letters, 35, 2008GL035 779, https://doi.org/10.1029/2008GL035779, 2008.

https://doi.org/10.5194/egusphere-2026-2794
Preprint. Discussion started: 11 June 2026
© Author(s) 2026. CC BY 4.0 License.

Percival, D. B. and Walden, A. T.: Spectral Analysis for Univariate Time Series, Cambridge University Press, 1 edn., https://doi.org/10.1017/9781139235723, 2020.

Plaut, G. and Vautard, R.: Spells of Low-Frequency Oscillations and Weather Regimes in the Northern Hemisphere, Journal of the Atmospheric Sciences, 51, 210–236, https://doi.org/10.1175/1520-0469(1994)051<0210:SOLFOA>2.0.CO;2, 1994.

Preisendorfer, R. W. and Mobley, C. D.: Principal Component Analysis in Meteorology and Oceanography, no. 17 in Developments in Atmospheric Science, Elsevier ; Distributors for the U.S. and Canada, Elsevier Science Pub. Co, Amsterdam ; New York : New York, NY, U.S.A, 1988.

Rasmusson, E. M. and Carpenter, T. H.: Variations in Tropical Sea Surface Temperature and Surface Wind Fields Associated with the Southern Oscillation/El Niño, Monthly Weather Review, 110, 354–384, https://doi.org/10.1175/1520-0493(1982)110<0354:VITSST>2.0.CO;2, 1982.

Rasmusson, E. M., Wang, X., and Ropelewski, C. F.: The Biennial Component of ENSO Variability, Journal of Marine Systems, 1, 71–96, https://doi.org/10.1016/0924-7963(90)90153-2, 1990.

Raynaud, D., Barnola, J.-M., Chappellaz, J., Blunier, T., Indermühle, A., and Stauffer, B.: The Ice Record of Greenhouse Gases: A View in the Context of Future Changes, Quaternary Science Reviews, 19, 9–17, https://doi.org/10.1016/S0277-3791(99)00082-7, 2000.

Rayner, N. A., Parker, D. E., Horton, E. B., Folland, C. K., Alexander, L. V., Rowell, D. P., Kent, E. C., and Kaplan, A.: Global Analyses of Sea Surface Temperature, Sea Ice, and Night Marine Air Temperature since the Late Nineteenth Century, Journal of Geophysical Research: Atmospheres, 108, 2002JD002 670, https://doi.org/10.1029/2002JD002670, 2003.

Salzer, M. W., Bunn, A. G., Graham, N. E., and Hughes, M. K.: Five Millennia of Paleotemperature from Tree-Rings in the Great Basin, USA, Climate Dynamics, 42, 1517–1526, https://doi.org/10.1007/s00382-013-1911-9, 2014.

Saraswati, A. T. and de Viron, O.: Anitasaraswati/MSSAkit: MSSAkit v1.0.0, Zenodo, https://doi.org/10.5281/ZENODO.10377708, 2023.

Sarnthein, M., Van Kreveld, S., Erlenkeuser, H., Grootes, P. M., Kucera, M., Pflaumann, U., and Schulz, M.: Centennial-to-millennial-scale Periodicities of Holocene Climate and Sediment Injections off the Western Barents Shelf, 75°N, Boreas, 32, 447–461, https://doi.org/10.1111/j.1502-3885.2003.tb01227.x, 2003.

Schilt, A., Baumgartner, M., Schwander, J., Buiron, D., Capron, E., Chappellaz, J., Loulergue, L., Schüpbach, S., Spahni, R., Fischer, H., and Stocker, T. F.: Atmospheric Nitrous Oxide during the Last 140,000years, Earth and Planetary Science Letters, 300, 33–43, https://doi.org/10.1016/j.epsl.2010.09.027, 2010.

Schmeits, M. J. and Dijkstra, H. A.: Physics of the 9-Month Variability in the Gulf Stream Region: Combining Data and Dynamical Systems Analyses, Journal of Physical Oceanography, 30, 1967–1987, https://doi.org/10.1175/1520-0485(2000)030<1967:POTMVI>2.0.CO;2, 2000.

Schulz, M., Prange, M., and Klocker, A.: Low-Frequency Oscillations of the Atlantic Ocean Meridional Overturning Circulation in a Coupled Climate Model, Climate of the Past, 3, 97–107, https://doi.org/10.5194/cp-3-97-2007, 2007.

Seitola, T., Silén, J., and Järvinen, H.: Randomised Multichannel Singular Spectrum Analysis of the 20th Century Climate Data, Tellus A: Dynamic Meteorology and Oceanography, 67, 28 876, https://doi.org/10.3402/tellusa.v67.28876, 2015.

Sévellec, F., Huck, T., and Jelloul, M.: On the Mechanism of Centennial Thermohaline Oscillations, Journal of Marine Research, 64, 2006.

Slawinska, J. and Robock, A.: Impact of Volcanic Eruptions on Decadal to Centennial Fluctuations of Arctic Sea Ice Extent during the Last Millennium and on Initiation of the Little Ice Age, Journal of Climate, 31, 2145–2167, https://doi.org/10.1175/JCLI-D-16-0498.1, 2018.

Taricco, C., Mancuso, S., Ljungqvist, F. C., Alessio, S., and Ghil, M.: Multispectral Analysis of Northern Hemisphere Temperature Records over the Last Five Millennia, Climate Dynamics, 45, 83–104, https://doi.org/10.1007/s00382-014-2331-1, 2015.

https://doi.org/10.5194/egusphere-2026-2794
Preprint. Discussion started: 11 June 2026
© Author(s) 2026. CC BY 4.0 License.

Te Raa, L. and Dijkstra, H. A.: Modes of Internal Thermohaline Variability in a Single-Hemispheric Ocean Basin, Journal Of Marine Research, 61, 491–516, 2003.

Te Raa, L., Gerrits, J., and Dijkstra, H. A.: Identification of the Mechanism of Interdecadal Variability in the North Atlantic Ocean, Journal of Physical Oceanography, 34, 2792–2807, https://doi.org/10.1175/JPO2655.1, 2004.

Thomson, D.: Spectrum Estimation and Harmonic Analysis, Proceedings of the IEEE, 70, 1055–1096, https://doi.org/10.1109/PROC.1982.12433, 1982.

Torrence, C. and Compo, G. P.: A Practical Guide to Wavelet Analysis, Bulletin of the American Meteorological Society, 79, 61–78, https://doi.org/10.1175/1520-0477(1998)079<0061:APGTWA>2.0.CO;2, 1998.

Vautard, R. and Ghil, M.: Singular Spectrum Analysis in Nonlinear Dynamics, with Applications to Paleoclimatic Time Series, Physica D: Nonlinear Phenomena, 35, 395–424, https://doi.org/10.1016/0167-2789(89)90077-8, 1989.

Vellinga, M. and Wu, P.: Low-Latitude Freshwater Influence on Centennial Variability of the Atlantic Thermohaline Circulation, Journal of Climate, 17, 4498–4511, https://doi.org/10.1175/3219.1, 2004.

Waldman, R., Hirschi, J., Voldoire, A., Cassou, C., and Msadek, R.: Clarifying the Relation between AMOC and Thermal Wind: Application to the Centennial Variability in a Coupled Climate Model, Journal of Physical Oceanography, 51, 343–364, https://doi.org/10.1175/JPO-D-19-0284.1, 2021.

Winton, M.: Energetics of Deep-Decoupling Oscillations, Journal of Physical Oceanography, 25, 420–427, https://doi.org/10.1175/1520-0485(1995)025<0420:EODDO>2.0.CO;2, 1995.

Yang, K., Yang, H., and Li, Y.: A Theory for Self-Sustained Multicentennial Oscillation of the Atlantic Meridional Overturning Circulation. Part II: Role of Temperature, Journal of Climate, 37, 913–926, https://doi.org/10.1175/JCLI-D-22-0755.1, 2024a.

Yang, K., Yang, H., Li, Y., and Zhang, Q.: North Atlantic Ocean–Originated Multicentennial Oscillation of the AMOC: A Coupled Model Study, Journal of Climate, 37, 2789–2807, https://doi.org/10.1175/JCLI-D-23-0422.1, 2024b.

Zhong, Y., Miller, G. H., Otto-Bliesner, B. L., Holland, M. M., Bailey, D. A., Schneider, D. P., and Geirsdottir, A.: Centennial-Scale Climate Change from Decadally-Paced Explosive Volcanism: A Coupled Sea Ice-Ocean Mechanism, Climate Dynamics, 37, 2373–2387, https://doi.org/10.1007/s00382-010-0967-z, 2011.

Zhu, F., Emile-Geay, J., McKay, N. P., Hakim, G. J., Khider, D., Ault, T. R., Steig, E. J., Dee, S., and Kirchner, J. W.: Climate Models Can Correctly Simulate the Continuum of Global-Average Temperature Variability, Proceedings of the National Academy of Sciences, 116, 8728–8733, https://doi.org/10.1073/pnas.1809959116, 2019.